Available online at www.sciencedirect.com
ScienceDirect
Journal of the Mechanics and Physics of Solids
55 (2007) 1053–1085

JOURNAL OF THE MECHANICS AND PHYSICS OF SOLIDS

www.elsevier.com/locate/jmps

# Analyses of tensile deformation of nanocrystalline $\alpha$-$Fe_2O_3$ + *fcc*-Al composites using molecular dynamics simulations

Vikas Tomar[a,*], Min Zhou[b]

[a]*Department of Aerospace and Mechanical Engineering, University of Notre Dame, Notre Dame, IN 46556, USA*
[b]*George W. Woodruff School of Mechanical Engineering, Georgia Institute of Technology, Atlanta, GA 30332-0405, USA*

Received 18 March 2006; received in revised form 8 September 2006; accepted 16 October 2006

**Abstract**

The tensile deformation of nanocrystalline $\alpha$-$Fe_2O_3$ + *fcc*-Al composites at room temperature is analyzed using molecular dynamics (MD) simulations. The analyses focus on the effects of variations in grain size and phase volume fraction on strength. For comparison purposes, nanostructures of different phase volume fractions at each grain size are given the same grain morphologies and the same grain orientation distribution. Calculations show that the effects of the fraction of grain boundary (GB) atoms and the electrostatic forces between atoms on deformation are strongly correlated with the volume fractions of the Al and $Fe_2O_3$ phases. In the case of nanocrystalline Al where electrostatic forces are absent, dislocation emission initiates primarily from high-angle GBs. For the composites, dislocations emits from both low-angle and high-angle GBs due to the electrostatic effect of Al–$Fe_2O_3$ interfaces. The effect of the interfaces is stronger in structures with smaller average grain sizes primarily because of the higher fractions of atoms in interfaces at smaller grain sizes. At all grain sizes, the strength of the composite lies between those of the corresponding nanocrystalline Al and $Fe_2O_3$ structures. Inverse Hall–Petch (H–P) relations are observed for all structures analyzed due to the fact that GB sliding is the dominant deformation mechanism. The

*Corresponding author. Tel.: +1 574 631 7826; fax: +1 574 631 8341.
*E-mail addresses:* vikas.tomar@nd.edu (V. Tomar), min.zhou@gatech.edu (M. Zhou).

0022-5096/$ - see front matter 
doi:10.1016/j.jmps.2006.10.005

slopes of the inverse H–P relations are strongly influenced by the fraction of GB atoms, atoms associated with defects, and the volume fractions of the Al and $Fe_2O_3$ phases.


*Keywords:* Molecular dynamics; Nanocrystalline composites; Hall-Petch; Grain boundaries

## 1. Introduction

Because they depend on phenomenological descriptions of interatomic interactions, classical molecular dynamics (MD) simulations are appropriate only in the domain of properties to which the interatomic potentials are fitted. MD simulations also face limitations in time scale (of the order of nanoseconds) and length scale (of the order of nanometers). Despite these limitations, MD has proven to be a very useful tool for analyzing deformation mechanisms and for predicting qualitative trends of the dependence of mechanical strength of nanophase materials on their phase morphology. For example, the MD results of Yamakov et al. (2002a) on deformation twinning in nanocrystalline Al with grain sizes from 30 to 90 nm have been found to be in close agreement with experimental observations reported by Liao et al. (2003a) and Liao et al. (2003b). MD simulations have provided phenomenological trends on deformation mechanisms of nanocrystalline and nanophase materials in agreement with experiments, see for example Kadau et al. (2002), Abraham (2003), and Buehler et al. (2004). Recently, MD simulations have been used to achieve nm/cycle fatigue crack extension rates similar to what is observed in experiments, cf. Farkas et al. (2005).

Through MD simulations, it has been established that the room temperature deformation mechanisms of nanocrystalline materials fall into three main categories (cf. Hahn et al. (1997); Hahn and Padmanabhan (1997); Konstantinidis and Aifantis (1998); Van Swygenhoven et al. (2001); Derlet et al. (2003); Fedorov et al. (2003); Gutkin et al. (2003), and Kumar et al. (2003)). These are;

(i) inter-granular mechanisms consisting of uncorrelated atom shuffling events at high-angle grain boundaries (GBs) resulting in grain boundary (GB) sliding;
(ii) intra-granular mechanisms such as partial dislocation emission and twinning in nanocrystalline metals with grain sizes larger than 10 nm; and
(iii) cooperative grain behaviors, i.e. micro-shear banding or rotation of clusters of grains.

MD simulations have also been used in the study of fracture phenomena for many years, cf. Abraham (2003), Latapie and Farkas (2004), and Buehler (2006). One of the key focus areas in nanomaterials technology is the development of nanocrystalline materials with desired mechanical, thermal, and electrical properties. $Al + Fe_2O_3$ nanocomposites synthesized through a sol–gel process (Tillotson et al.,2001) are one example that offers the promise of combined chemical reactivity and mechanical strength when mixed with appropriate nanoscopic reinforcements such as epoxy, cf. Granier and Pantoya (2004). For this composite material system, a systematic study of the effects of phase morphology on mechanical strength is needed. Specifically, changes in the nucleation and propagation of defects (such as dislocations) with variations in nanoscale phase morphology and their

effects on strengths need to be characterized. Such a study is carried out here using classical MD. Most MD simulations on nanocrystalline materials have been performed on fully dense *fcc* or *bcc* metals (primarily Pd, Ni, Al, Au, Fe, and Cu). The samples are usually free from impurities with adjacent grains separated primarily by high-angle GBs. Few MD analyses have been carried out for nanocrystalline composite materials. The primary reason is the lack of interatomic potentials that describe the properties of individual phases as well as interactions at interfaces between different phases. Recently, an interatomic potential for *fcc*-Al + $\alpha$-$Fe_2O_3$ material system is developed by Tomar and Zhou (2004), Tomar (2005), and Tomar and Zhou (2006a). Using this potential, Tomar and Zhou (2006b) have analyzed tension–compression strength asymmetry in $\alpha$-$Fe_2O_3$ + *fcc*-Al nanocrystalline composites. This potential is used for the analyses presented in this paper. The particular focus is on the quasistatic tensile deformation of nanocrystalline $\alpha$-$Fe_2O_3$ + *fcc*-Al composites with average grain sizes of 3.9, 4.7, and 7.2 nm. The term "quasistatic deformation" in an atomistic setting often implies energy minimization based on molecular statics at 0 K. Here, "quasistatic deformation" implies MD simulations of mechanical deformation with alternate steps of stretching and equilibration at a constant temperature (300 K) using NPT ensemble equations to approximate quasistatic deformation in the regular engineering laboratory sense. Nanostructures with prescribed log-normal grain size distributions and phase volume fractions are considered.

## 2. MD framework and interatomic potential

### 2.1. Framework of analysis

The simulations in this paper are carried out under 3D conditions (using periodic boundary conditions or PBCs). For comparison, nanocrystalline Al, $Fe_2O_3$, and Al + $Fe_2O_3$ composites with 40% and 60% Al by volume are considered. The focus is on understanding the deformation mechanisms in the composites and on delineating the factors affecting their strength. In the nanostructures used, the orientations of individual grains are chosen randomly. Consequently, a random distribution of low-angle and high-angle GBs is considered. The analyses are based on an interatomic potential developed by Tomar and Zhou (2006a) which uses electrostatic forces with electronegativity equalization. This results in extremely demanding requirements on the CPU time of the supercomputers used. Due to limited availability of computational resources, the analyses are judiciously planned to focus on the effects of (1) the phase volume fraction and (2) the grain size of the nanocrystalline composites on deformation.

To carry out the analyses, 12 different material samples are chosen (shown later), involving three different grains sizes (3.9, 4.7, and 7.2 nm) and four different compositions. These samples allow intergranular and intragranular deformation mechanisms to be analyzed. For example, in the case of nanocrystalline Al the fraction of GB atoms varies from 24.5% for structures with an average grain size of 7.2 nm to 51.65% for structures with an average grain size of 3.9 nm. With such variations in the fraction of GB atoms, inter-granular deformation mechanisms are expected to be relevant, in addition to intra-granular mechanisms due to dislocation activities. Although the difference between the 3.9 and 4.7 nm nanostructures in terms of average grain size is relatively small, the significant differences in the fractions of GB atoms and in the degrees of GB mismatches allow the effects of GB sizes and mismatches to be delineated. In addition to the analysis of the

behavior of the multiphase nanocomposites, this paper also reports results concerning the deformation behavior of nanocrystalline Al that go beyond the extent of analysis in the existing literature. Specifically, while it is known that the effect of dislocations on deformation mechanism is stronger in nanocrystalline materials with higher fractions of low-angle GBs (Van Swygenhoven et al.,1999) the differences between the effects of low-angle and high-angle GBs on dislocation emission in nanocrystalline materials have not been made clear. Most existing analyses have focused on other issues. For example, the analysis of Yamakov et al. (2002b) and Yamakov et al. (2004) on nanocrystalline Al is performed in a 2D columnar setting. The applicability of their results to 3D structures with random mismatches at GBs is unclear. Van Swygenhoven et al. (2006) analyzed a 3D nanocrystalline Al structure with a mean grain size of 12 nm without addressing the effect of grain size variation.

### 2.2. Interatomic potential

$\alpha$-$Fe_2O_3$ + *fcc*-Al nanocomposites form chemically active thermite mixtures. Therefore, the possibility of the formation of $Al_2O_3$, Fe and other intermediate states needs to be considered. Accordingly, the interatomic potential is required to simultaneously describe the behavior of $\alpha$-$Fe_2O_3$, *fcc*-Al, $\alpha$-$Al_2O_3$, and *bcc*-Fe. To state it differently, Al–Al, Fe–Fe, Al–Fe, Al–O, Fe–O, and O–O interactions and the coupling between these interactions must be accounted for. This task necessitates a functional form that allows multi-body, pairwise, and electrostatic interactions among different species to be described. Our approach is to first fit the potential parameters for the Al–Al, Fe–Fe, Al–O, Fe–O and O–O interactions to the lattice constants, elastic moduli, and cohesive energies of *fcc*-Al, *bcc*-Fe, $\alpha$-$Fe_2O_3$, and $\alpha$-$Al_2O_3$. To determine the Fe–Al parameters, the potential is then fitted to the lattice constants and cohesive energies of B2 Fe–Al. In addition to being fitted to the lattice constants, elastic constants, and cohesive energies, the potential gives predictions of the surface and stacking fault energies for the crystalline components that compare well with the predictions of established potentials in the literature for the corresponding crystalline components. Consequently, the potential is capable of simultaneously describing the crystalline properties of *fcc*-Al, *bcc*-Fe, B2 Fe–Al, $\alpha$-$Fe_2O_3$, and $\alpha$-$Al_2O_3$, cf. Tomar and Zhou (2004), Tomar (2005), and Tomar and Zhou (2006a). With this relatively general applicability, we surmise that the potential provides reasonable approximations of the Al–Al, Fe–Fe, Al–Fe, Al–O, Fe–O, and O–O interactions and their coupling in the presence of each other as may exist in a general system with a combination of these components. The functional form of the potential is a combination of existing potentials in the literature for the individual crystalline components, i.e.,

$$E^{\text{total}}(\mathbf{r},q)=\left\{\sum_i F_i\left(\sum_j[\rho_j(\mathbf{r}_{ij})]\right)+\frac{1}{2}\left(\sum_i\sum_j\phi_{ij}(\mathbf{r}_{ij})\right)_{i\neq j}\right\}_{\text{Glue}}+\left\{\sum_i E_{\text{es}}(\mathbf{r}_i,q_i)\right\}_{\text{Electrostatic}}. \tag{1}$$

In the above expression, $\mathbf{r}_i$ is the position vector of atom $i$ and $\mathbf{r}_{ij}$ is the distance between atoms $i$ and $j$. This potential expression contains a glue potential term ($E_{\text{glue}}$) similar to the

EAM potential with a generalized cluster functional (cf. Carlsson, 1990) and an electrostatic potential term ($E_{es}$) for second-order electrostatic interactions. The electrostatic interactions are considered for point charges located at atomic core centers as well as for diffused charges around the atomic cores. Specifically, for each atomic species (Al, Fe, or O) the total energy is a function of atomic position vector $\mathbf{r}$ and charges $q$ in the form

$$E(\mathbf{r},\ q) = E_{\text{glue}}(\mathbf{r}) + E_{\text{es}}(\mathbf{r},\ q)\cdot \tag{2}$$

Here,

$$E_{\text{glue}}(\mathbf{r}) = \sum_i F_i\left(\sum_j \rho_j\right) + \frac{1}{2}\sum_{i,j(i\neq j)} \phi_{ij}, \tag{3}$$

is the glue potential with a generalized cluster functional $F(\sum_j \rho_j)$ which depends on the embedding electron density $\rho$ and a pair interaction potential $\phi_{ij}$ and

$$\sum_i E_{\text{es}}(\mathbf{r}_i,\ q_i) = \sum_i q_i\chi_i + \frac{1}{2}\sum_{i,j(i\neq j)} q_i q_j V_{ij}, \tag{4}$$

is the electrostatic energy, $\chi$ is the instantaneous electronegativity, and $V$ is the electrostatic pair interaction potential. Fitting of the potential involves least-square minimization of the difference between the fitted values and actual values of the properties, cf. Tomar and Zhou (2004), Tomar (2005), and Tomar and Zhou (2006a). As described in these references, for an $Al + Fe_2O_3$ nanocomposite structure, the interatomic potential has an electrostatic term in the form of (in the following $\alpha$ stands for the Al, Fe or O species)

$$\begin{aligned} E^{\alpha}_{\text{ES}} = q_\alpha\left\{\chi^0_\alpha + \sum_{i(\text{Al}),j(\neq i)} Z_j\left[\int d^3\mathbf{r}\frac{f_\alpha(\mathbf{r})}{|\mathbf{r}-\mathbf{r}_j|} - \int d^3\mathbf{r}_1\int d^3\mathbf{r}_2\frac{f_\alpha(\mathbf{r}_1)f_j(\mathbf{r}_2)}{r_{12}}\right]\right\} \\ + \frac{1}{2}\left\{\sum_{i(\kappa)} q^2_\alpha J^0_\alpha + \sum_{i(\kappa),j(\neq i)} q_\alpha q_j\int d^3\mathbf{r}_1\int d^3\mathbf{r}_2\frac{f_\alpha(\mathbf{r}_1)f_j(\mathbf{r}_2)}{\mathbf{r}_{12}}\right\} \end{aligned} \tag{5}$$

a cluster functional term in the form of

$$F^\alpha = E^\alpha_0 A^\alpha\left[\left(\sum\rho^{\text{Al}} + \sum\rho^{\text{Fe}} + \sum\rho^{\text{O}}\right)\ln\left(\sum\rho^{\text{Al}} + \sum\rho^{\text{Fe}} + \sum\rho^{\text{O}}\right)\right]^{B^\alpha} \tag{6}$$

and a pair interaction term in the form of

$$\phi^\alpha_{\text{pair}} = \frac{1}{2}\sum_{i,j(j\neq i)}\left\{\begin{array}{l} \sum\limits_{\alpha,\ \beta}\psi^{\alpha-\beta}_0\left[\exp\left(-2\gamma^{\alpha-\beta}\left(\mathbf{r}-t^{\alpha-\beta}\right)\right) - 2\exp\left(-\gamma^{\alpha-\beta}\left(\mathbf{r}-t^{\alpha-\beta}\right)\right)\right] \\ \quad - \sum\limits_{\alpha,\ \beta}\psi^{\alpha-\beta}_0\left[\exp\left(-2\gamma^{\alpha-\beta}\left(D^{\alpha-\beta}-t^{\alpha-\beta}\right)\right) - 2\exp\left(-\gamma^{\alpha-\beta}\left(D^{\alpha-\beta}-t^{\alpha-\beta}\right)\right)\right] \\ \quad - \sum\limits_{\alpha,\ \beta}\frac{D^{\alpha-\beta}}{20}\left[1-\left(\frac{r}{D^{\alpha-\beta}}\right)^{20}\right]\left[\begin{array}{l} -2\gamma^{\alpha-\beta}\exp\left(-2\gamma^{\alpha-\beta}\left(D^{\alpha-\beta}-t^{\alpha-\beta}\right)\right) \\ +2\gamma^{\alpha-\beta}\exp\left(-\gamma^{\alpha-\beta}\left(D^{\alpha-\beta}-t^{\alpha-\beta}\right)\right)\end{array}\right] \end{array}\right\}. \tag{7}$$

$(\beta) = \{\text{Al},\ \text{Fe},\ \text{O}\}.$

In the Al phase of the composite, only $F^{\text{Al}}$ and $\phi^{\text{Al}}_{\text{pair}}$ terms are used. In these terms, Al–O and Al–Fe interactions are not considered. The parameters in these terms are obtained by fitting to the properties of *fcc*-Al. In the $Fe_2O_3$ phase of the composite, $E^{\text{Fe}}_{\text{ES}}$, $E^{\text{O}}_{\text{ES}}$, $F^{\text{Fe}}$, $F^{\text{O}}$,

$\phi^{Al}_{pair}$, and $\phi^{O}_{pair}$ terms are used. In these terms, Fe–Al and O–Al interactions are not considered. The parameters in these terms are obtained by fitting to the properties of $\alpha$-$Fe_2O_3$.

At interfaces between Al and $Fe_2O_3$, all terms above are considered along with an additional term $E^{Al}_{ES}$ which is used to account for the possibility that Al atoms may be oxidized under the effect of charged Fe and O atoms. Electronegativity equalization (cf. Strietz and Mintmire, 1994) is carried out to determine the charges of the Al, Fe, and O atoms in an interfacial region covered by the short-range electrostatic cutoff radius (10 Å). The value of 10 Å here is obtained by matching the values of the Coulomb energy and the Coulomb virial as a function of the short-range electrostatic cutoff. In addition, a convergence analysis for the variation in the electrostatic energy as a function of the short-range cutoff is carried out. The value of 10 Å satisfies both criteria. This choice of cutoff radius corresponds to a description of the homogeneous crystalline systems. It is possible that nanocrystalline grain deformation mechanisms may be affected by changes in the cutoff radius, see e.g., Ogata et al. (2000). In this respect, the use of the interatomic potential in nanocrystalline structures involves a degree of approximation. Other sources of approximation come from the use of a fixed set of parameters and functional forms to approximate a wide range of deformation modes for which, perhaps, quantum mechanical approach is the most suitable approach.

The electronegativity equalization is based on a description of the total electrostatic energy of an array of atoms as a function of the atomic charges (valences) and their positions, cf. Strietz and Mintmire (1994). With the consideration of all $E^{Al}_{ES}$, $E^{Fe}_{ES}$, $E^{O}_{ES}$, $F^{Al}$, $F^{Fe}$, $F^{O}$, $\phi^{Al}_{pair}$, $\phi^{Fe}_{pair}$, and $\phi^{O}_{pair}$ terms, the behavior of Al, Fe, and O atoms at Al–$Fe_2O_3$ interfaces can be accounted for. This procedure for calculating interatomic interactions in a composite represents an approximation and is one of the underlying assumptions of the MD framework here. The potential is specific to Al–Al, Fe–Fe, Al–Fe, Al–O, Fe–O, and O–O interactions with parameters fitted to *fcc*-Al, *bcc*-Fe, $\alpha$-$Al_2O_3$ and $\alpha$-$Fe_2O_3$. The required fitting of all combinations of Al/Fe/O species to obtain bulk properties such as crystal lattice parameters, elastic constants, the surface energies and stacking fault energies of *fcc*-Al, *bcc*-Fe, $\alpha$-$Al_2O_3$ and $\alpha$-$Fe_2O_3$ represents a fairly large database. Therefore, the potential is regarded as reasonable for application to *fcc*-Al + $\alpha$-$Fe_2O_3$ composites. The accuracy for application to other polymorphs of alumina or of iron-oxide is unknown, and, therefore, is not automatically recommended. Within this context, we surmise that the reasonable approximations of the Al–Al, Fe–Fe, Al–Fe, Al–O, Fe–O, and O–O interactions through fitting to the individual phase properties and consideration of the coupling of these interactions in the presence of each other using electronegativity equalization make it possible to describe interatomic interactions in a system that consists of a combination of the individual phases directly analyzed. A more accurate description of both composite structures and various polymorphs would involved more extensive fitting which perhaps can be the subject of a future paper. Such an endeavor can certainly benefit from more extensive ab initio calculations. Alternatively, it may be better pursued in a first principles setting.

The potential parameters are determined by fitting the functional form to the lattice constants, cohesive energies, and elastic constants of *fcc*-Al, *bcc*-Fe, $\alpha$-$Al_2O_3$ and $\alpha$-$Fe_2O_3$. The parameters related to the Fe–Al pair interactions are determined by fitting to the formula unit energy of B2-FeAl. The fitting process involves the least-square minimization of the sum of squared differences between target property values (experimental or ab

initio) and values calculated from a trial parameter set. Calculations of the elastic constants are based on the work of Catlow and Mackrodt (1982) who use the Born and Huang (1954) theory of crystal lattice. Their main contribution is the inclusion of crystal symmetry to speed up calculations. Temperature is not explicitly considered in this formulation. Instead, the fitting is assumed to be carried out at the temperature at which the properties are specified. We use properties specified at 300 K. Tables 1–5 in Tomar and Zhou (2006a) show the properties of *fcc*-Al, *bcc*-Fe, $\alpha$-$Al_2O_3$ and $\alpha$-$Fe_2O_3$ used during fitting. The tables also show values of the lattice constants, elastic constants, and cohesive energies predicted by the potential. Reasonable agreement is seen between the predicted values and the experimental/ab initio values. In the case of *fcc*-Al, the fitting fares better than the potential of Voter and Chen (1987). In the case of *bcc*-Fe, the fitting is comparable to the predictions made by the potential of Farkas et al. (2001). In the case of $\alpha$-$Al_2O_3$, the fitted properties compare well with the values provided by Strietz and Mintmire (1994). For $\alpha$-$Fe_2O_3$, no comparable interatomic potential is available. Accordingly, the properties are compared to the experimental values provided by Huntington (1958). Overall, the predictions compare well with established potentials for the individual crystalline components, cf. Tomar and Zhou (2006a).

The potential is implemented in a modified version of the scalable parallel MD code DL_POLY 2.14 (Smith et al., 2002) which uses the atom-decomposition paradigm (Vincent and Merz, 1995) for high performance computing. The graphics are generated using VMD (cf. Humphrey et al.,1996). There are three "structural" defect visualization schemes that have been used (and are available) for identifying defects in deforming nanocrystalline structures. The word "structural" refers to defect identification based on the change in neighboring atomic positions within a pre-specified cutoff. These schemes use (1) the centrosymmetry parameter by Kelchner et al. (1998), (2) the common neighbor analyses (CNA) parameter by Honeycutt and Anderson (1987), and (3) the slip-vector magnitude parameter by Zimmerman et al. (2001).

The centrosymmetry parameter is not useful in a nanocrystalline setting for identifying GBs, cf. Rodríguez de la Fuente et al. (2002). The CNA has been used to identify the motion of dislocations through GBs by Van Swygenhoven and Caro (1997). However, CNA is not appropriate for identifying the magnitude of Burger's vectors. The slip-vector approach has been used by Zimmerman et al. (2001) and Rodríguez de la Fuente et al. (2002) to identify dislocations and to analyze the magnitude of Burger's vectors during nanoindentation. In this paper, visualization is primarily aimed at identifying the extent of dislocation emission at low-angle and high-angle GBs that result in stacking fault formation. The focus is also on outlining the motions of GB atoms during deformation. For this purpose, the slip-vector approach is most appropriate. Fig. 1(a) shows a cross section of a nanocrystalline Al sample with GB mismatches outlined by broken and solid lines. The $\{1\,0\,0\}$-$\{1\,0\,0\}$ low-angle mismatch GB is shown with a broken line. The $\{1\,0\,0\}$-$\{1\,1\,0\}$, $\{1\,1\,0\}$-$\{1\,1\,0\}$, $\{1\,1\,0\}$-$\{1\,1\,1\}$, and $\{1\,1\,1\}$-$\{1\,0\,0\}$ high-angle mismatch GBs are shown with solid lines. Fig. 1(b) shows GBs at the same cross-section with atoms colored using the slip-vector approach. The corresponding color scale is also shown. In Al, the unit glissile dislocation is the $a/2[1\,1\,0]$ dislocation with a Burger's vector magnitude of 2.87 Å which is close to the upper limit of the slip-vector scale shown in Fig. 1(b). For clarity, the figure shows only those atoms that have slip vector magnitudes above 0.25, eliminating the atoms that occupy bulk lattice positions. Clearly, the slip-vector approach allows atoms in GBs to be differentiated from atoms inside grains.

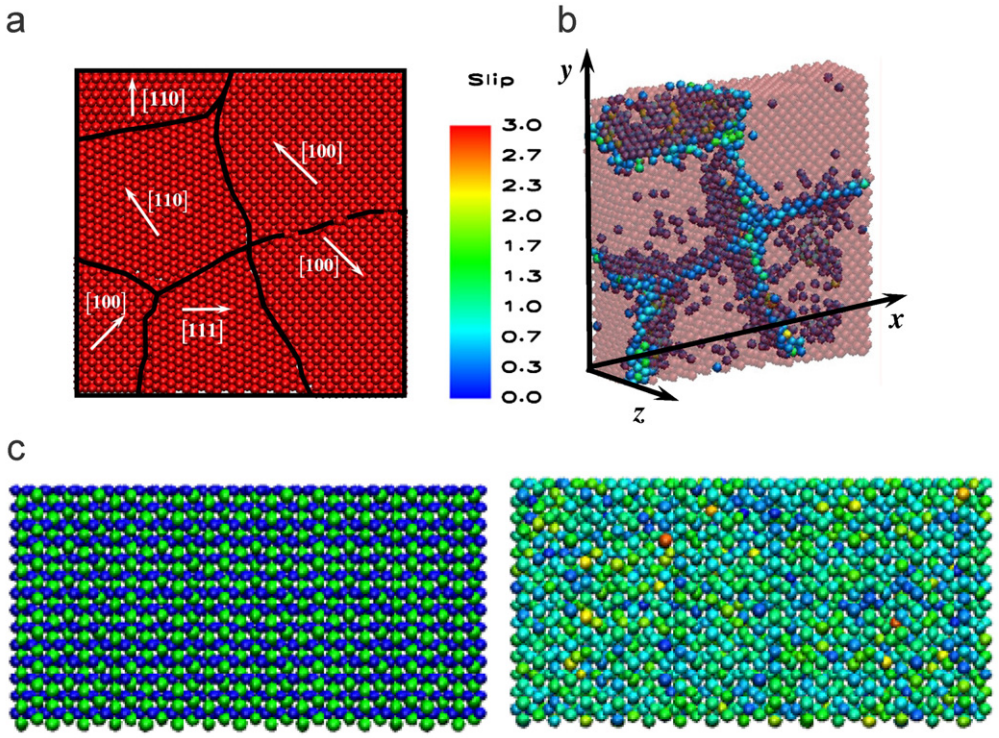


Fig. 1. (a) identification of GB mismatch in nanocrystalline Al with an average grain size of 7.2 nm (broken lines are low-angle GBs and solid lines are high-angle GBs), (b) identification of GBs using the slip vector approach (atoms in GBs have slip vector value greater than 0.25), and (c) demonstration of the slip vector approach based visualization for $\langle 0\,0\,0\,1 \rangle$ oriented (horizontal axis) single crystalline $Fe_2O_3$.

In the case of $Fe_2O_3$, all three visualization approaches fail to yield any structural pattern. The primary reason is the difference between the cubic unit cell structure for Al and the rhombohedral primitive unit cell structure for $Fe_2O_3$. For example, a hexagonal $Fe_2O_3$ supercell after 10 ps of MD equilibration is shown in Fig. 1(c). The left-hand image is the structure with atoms colored by their types and the right-hand image shows the same structure with the atoms colored by the magnitude of the slip-vector. No clear structural pattern is visible. It is clear that the slip-vector based visualization approach fails even in the case of single crystalline $Fe_2O_3$. The use of other visualization approaches also did not provide a clear structural visualization of defects in single crystalline $Fe_2O_3$. Since the $Fe_2O_3$ phase is found to be amorphous at the lengthscale of analyses here, the partial and the total radial distribution functions (RDFs) are extensively used to identify the structural order.

The partial RDF for an atomic pair $\alpha$–$\beta$, $g\alpha_\beta$, is determined from

$$g_{\alpha,\beta} = \frac{\langle n_{\alpha,\beta}(\mathbf{r},\ \mathbf{r}+\Delta\mathbf{r})\rangle}{4\pi\mathbf{r}^2\Delta\mathbf{r}}\frac{V}{N_\beta}, \quad (\alpha,\ \beta = \text{atom } 1,\ \text{atom } 2)\cdot \tag{8}$$

Here, $\langle n_{\alpha,\beta}(\mathbf{r},\mathbf{r}+\Delta\mathbf{r})\rangle$ denotes the average number of particles of species $\beta$ surrounding a particle of species $\alpha$ in a spherical shell between $\mathbf{r}$ and $\mathbf{r}+\Delta\mathbf{r}$, $N_\beta$ is the total number of

particles of species $\beta$, and $V$ is the volume of system. For calculating the total $Fe_2O_3$ RDF, the partial Fe–Fe, Fe–O and O–O RDFs are summed up together. Partial Al–Al and total $Fe_2O_3$ RDFs are used to identify changes in structural order during deformation.

## 3. Generation of the nanocrystalline structures

The nanocrystalline structures generated and used for deformation analyses are listed in Table 1. As illustrated in Fig. 2, these structures have three different average grain sizes (7.2, 4.7 and 3.9 nm) and four different volume fractions of the Al phase (100%, 60%, 40%, and 0%). The nanocrystalline structures of Al, $\alpha$-$Fe_2O_3$, and their composites (60% *fcc*-Al + 40% $\alpha$-$Fe_2O_3$ and 40% *fcc*-Al + 60% $\alpha$-$Fe_2O_3$) with the same average grain size have the same grain orientation and the same grain size distributions. For a particular average grain size (for example 7.2 nm) there are four different nanocrystalline structures with four different Al ($Fe_2O_3$) volume fractions. This allows for an analysis of the effect of

Table 1
Compositions and grain sizes of the nanostructures analyzed

| Pure Al | | | Pure $Fe_2O_3$ | | | 60% Al + 40% $Fe_2O_3$ | | | 40% Al + 60% $Fe_2O_3$ | | |
|---|---|---|---|---|---|---|---|---|---|---|---|
| PA1 | PA2 | PA3 | PHt1 | PHt2 | PHt3 | NCP641 | NCP642 | NCP643 | NCP461 | NCP462 | NCP463 |
| 7.2 | 4.7 | 3.9 | 7.2 | 4.7 | 3.9 | 7.2 | 4.7 | 3.9 | 7.2 | 4.7 | 3.9 |

Composition is in volume fraction of phases and average grain size is in nm.

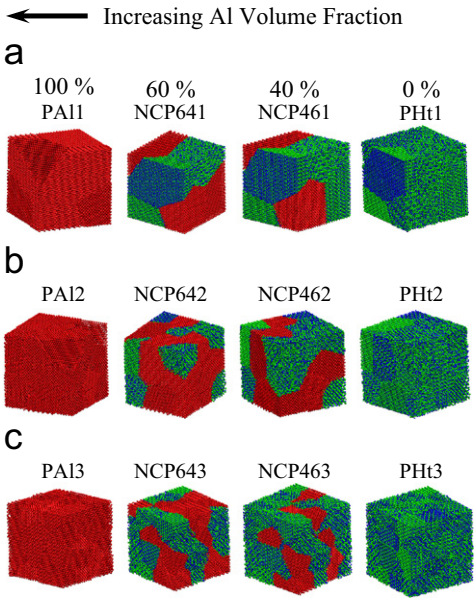


Fig. 2. Nanocrystalline structures in with different Al volume fractions and grain sizes of (a) 7.2 nm, (b) 4.7 nm, and (c) 3.9 nm (Al atoms are red, Fe atoms are blue, and O atoms are green).

variation in phase volume fraction on the deformation behavior. Simulations of the structures with three different grain sizes helped in an additional analysis of the effect of grain size variation. Accordingly, the focus of the analyses reported in the manuscript is on

(1) the analyses of the effect of variations in the phase volume fraction of the nanocrystalline composites on the deformation characteristics; and
(2) the analyses of the effect of grain size variation of the nanocrystalline composites on the deformation characteristics.

Overall, the analyses focus on the effects of variations in grain size and phase volume fraction on the strengths of nanocrystalline Al, $Fe_2O_3$, and $Al + Fe_2O_3$ composites with 40% and 60% Al by volume. The structures are generated by growing grains inside a cubic box. To approximate the behavior of bulk materials, the box is repeated in all three directions by imposing PBCs. The imposition of PBCs results in a nanocrystalline structure that has unimodal distribution of grain sizes. The size of the cubic box determines the maximum number of atoms that can be accommodated. This maximum number of atoms is limited by factors such as the memory and the CPU time required for carrying out MD simulations at timescales of the order of picoseconds. Accounting for these considerations, the size of the cubic box is kept at $10 \times 10 \times 10$ nm so that the maximum number of atoms does not exceed 100,000. The use of electrostatic forces with electronegativity equalization imposes extremely demanding requirements on the CPU time of the supercomputers used in the research. For a system with 100,000 atoms the uniaxial deformation calculations for one nanocrystalline structure took approximately 10 days. A total of approximately 200,000 h of supercomputing were used to obtain the results reported in this manuscript. Under the resource limitations, only systems with up to 100,000 atoms are analyzed. With this limitation, the largest grain size obtained by the bi-division of the cubic box in all three-dimensions (a total of 8 grains) is approximately 8.2 nm with the average grain size being 7.2 nm.

Approaches frequently used for generating nanocrystalline structures are the monodispersive grain growth method; cf. Gleiter (2000), the melt growth method, cf. Keblinski et al. (1998); and the Voronoi tessellation method, cf. Voronoi (1908), Chen (1995), and Schiøtz et al. (1999). The monodispersive grain growth technique is non-statistical in nature. The Voronoi tessellation method follows a fixed Voronoi–Poisson grain-size distribution which is rarely observed in experiments, cf. Gross and Li (2002). However, mesoscale simulations show that a Voronoi starting structure evolves very quickly towards (but never reaches) a log-normal distribution, cf. Haslam et al. (2001). Gross and Li (2002) combined the Monte-Carlo method with the Voronoi tessellation method for grain-growth to generate nanocrystalline structures with specified distributions of grain size. This procedure is also similar to that of Chen (1995). We follow a similar procedure here. The desired grain size distribution is log-normal with a 10% standard deviation. We generated nanocrystalline structures with three different average grain sizes: (1) structures with 8 grains and an average grain size of 7.2 nm; (2) structures with 27 grains and an average grain size of 4.7 nm; and (3) structures with 64 grains and an average grain size of 3.9 nm. For the generation of nanocrystalline composites, the constituent volume fraction is incorporated using a random number generator. A constituent is allocated a grain growth nucleus based on the value of a random number generated depending on the position of the nucleus in the cubic box. For the growth of each grain, one of the three orientations

([0 0 1], [0 1 0], or [0 0 1]) is selected randomly using another random number generator. In addition, other constraints are imposed such that the orientations of neighboring grains are always different from each other and that maximum possible mixing of the Al and the $Fe_2O_3$ phases is achieved. All structures generated follow log-normal grain size distributions with a 10% standard deviation.

Fig. 3 shows the histograms for the actual grain size distributions in the nanostructures and the corresponding prescribed log-normal and normal distributions. These geometrically generated structures are subjected to MD equilibration for 10 ps at 300 K in a manner similar to the what is used by Chen (1995), Van Swygenhoven and Caro (1998), and Schiøtz et al. (1999). This procedure is needed for obtaining equilibrated stress-free structures.

Configurations of the Al structures (PAl1, PAl2, and PAl3) after the MD equilibration are shown in Fig. 4. In order to compare the movement of the atoms in the grains and along GBs, only the cross-sections at the middle of the samples are shown. The orientation of each grain on the cross-section is also shown in Fig. 4(a). In Fig. 4, each sample contains randomly oriented grains in such a way that the GBs have a mix of the low-angle and high-angle mismatches. For convenience, the low-angle and high-angle mismatches are clearly outlined in the configurations before MD equilibration, see Fig. 4(a). The configurations after equilibration are shown in Fig. 4(b). During the MD equilibration, atomic movement in all samples is primarily along the GBs. The contributions of GB atoms to the overall deformation are analyzed with a distinction made between low-angle GBs and high-angle GBs. Note that the thickness of high-angle GBs is larger than that of low-angle GBs. In PAl1 and PAl2, GBs with {1 0 0}–{1 1 1} high-angle mismatches have the largest thickness. In PAl3, GBs with {1 1 0}–{1 1 1} and {1 1 0}–{1 0 0} high-angle mismatches have the largest thickness. These thickness values vary from 1 nm in PAl1 to ~2 nm in PAl3. A larger thickness indicates a higher amount of atomic movements along the GBs. High-angle GBs have greater mismatches along interfaces than those at low-angle GBs. Accordingly, atoms along high-angle GBs need to displace more than those along low-angle GBs. The composition gradient (spatial rate of change in structure from interface to regular lattice) along high-angle GBs is higher than that along low-angle GBs. This results in high-angle GBs having higher thicknesses. As a result, the probability of dislocation emission from high-angle GBs is higher. This deduction is discussed in more detail later in Section 5 during the analysis on the deformation of nanocrystalline Al.

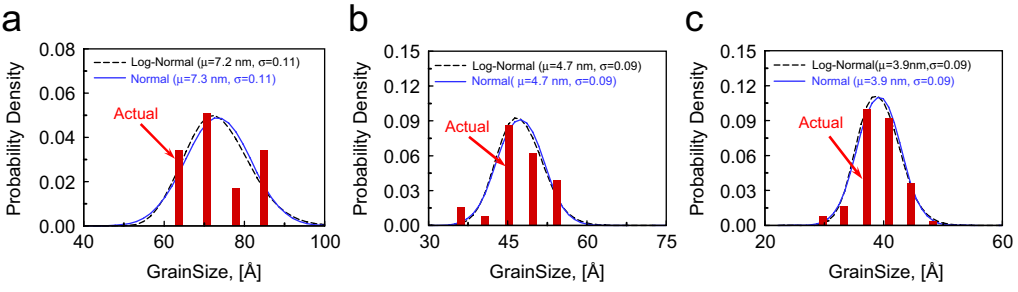


Fig. 3. A comparison of actually obtained grain size distributions and prescribed log-normal and normal distributions with average grain sizes of (a) 7.2 nm, (b) 4.7 nm, and (c) 3.9 nm.

Fig. 5 shows the fraction of GB atoms as a function of average grain size. The fraction is calculated based on the number of atoms with slip-vector magnitudes above 0.25. Based on the same classification, GBs are identified separately from bulk crystalline atoms in Fig. 1(b). A sharp non-linear increase is seen as the grain size is reduced. In particular, the fraction for PAl1 is 25%, whereas the fraction for PAl3 is approximately 52%. Tjong and

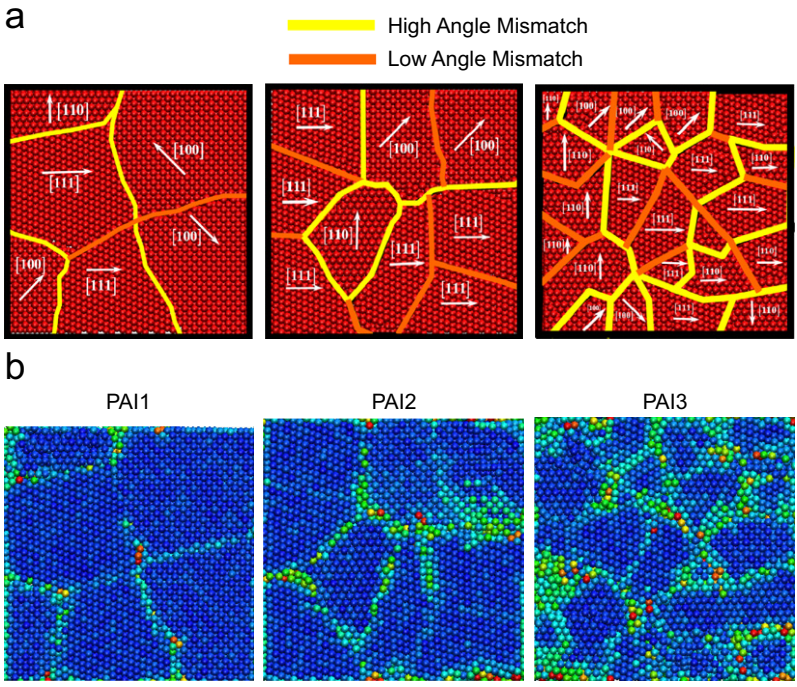


Fig. 4. (a) Low-angle and high-angle GB mismatches in Al structures before MD equilibration (line with light shades are high-angle GBs and lines with dark shades are low-angle GBs), (b) the same structures after equilibration with atoms colored using the slip-vector approach to outline GBs. Images shown are mid cross-sections.

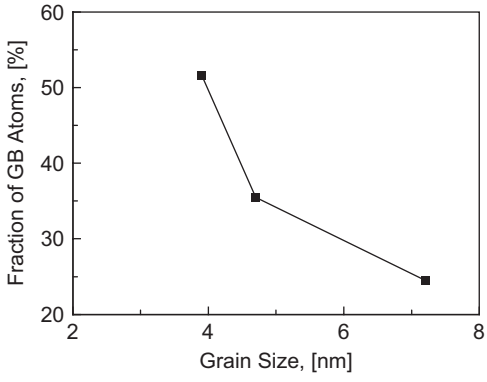


Fig. 5. The fraction of GB atoms as a function of average grain size for Al after MD equilibration.

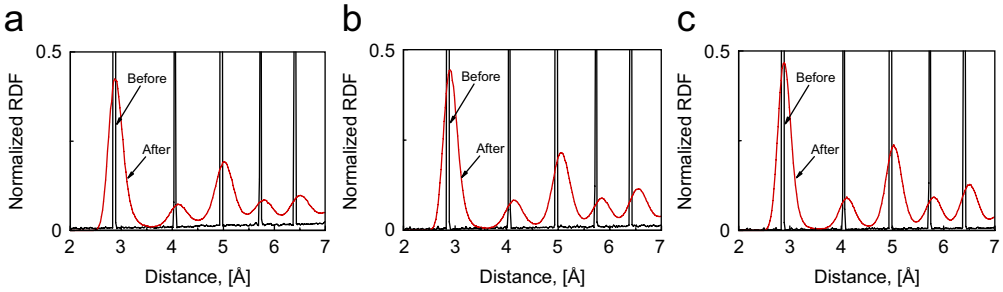


Fig. 6. A comparison of the partial Al–Al RDFs for Al structures with grain sizes of (a) 3.9 nm, (b) 4.7 nm, and (c) 7.2 nm, before and after MD equilibration.

Chen (2004) observed that at an average grain diameter of 5 nm the fraction is ~49%. The increase in the fraction of GB atoms with reduction in the grain size is attributed to the increase in surface area of grains available for interfacing with the neighboring grains and to the increase in the number of neighboring grains which in turn affects the factors such as the presence of disclinations and triple junctions. There is no experimental or theoretical evidence in favor or against the sharp increase. We speculate that this sharp increase is associated with the way the Voronoi tessellated structures are generated and admit it as a feature of the nanocrystalline structure generation procedure. The trend in Fig. 5 is primarily attributed to the increase in the surface area of a grain as its size decreases. To state it differently, the surface-to-volume ratio of a grain increases as the grain size decreases. Obviously, this increase in GB atom fraction will have a significant impact on the behavior of the material.

In Fig. 6, the partial Al–Al radial distribution functions (RDFs) before and after the MD equilibration for all nanocrystalline Al structures are shown. The RDFs differ from that of a perfect *fcc*-Al crystal before and after equilibration in two ways. First, the peaks are not sharp delta functions and are somewhat smeared even before equilibration due to a degree of mismatch along the GBs. Second, the RDFs do not approach zero after the first two peaks. The broadening of the RDF peaks after equilibration is in part due to the strain fields inside the grains (originating from the GBs) and in part due to atoms in or near the GBs sitting close to (but not at) the lattice positions. The fact that the RDF does not go to zero between the peaks denotes a disorder which in this case comes from the GBs. The average depth of the RDF valleys decreases with the average grain size. Clearly, this is due to the fact that at small grain sizes the fraction of atoms in GBs is higher. PAl1 has a higher fraction of atoms in bulk *fcc*-Al crystalline order and therefore sharper RDF peaks than PAl2 and PAl3. Similar features are observed for all structures as well. This observation clearly indicates that deformation mechanism will show a shift from being dislocation dominated for PAl1 to being GB sliding dominated for PAl3.

### 3.1. *Nanocrystalline $Fe_2O_3$ and Al+$Fe_2O_3$ composites after MD equilibration*

Fig. 7 shows the mid cross-sections of PHt1 before and after MD equilibration. A significant degree of loss in structural order after equilibration is clearly visible. Fig. 7(a) shows the effective distances of influence for atoms along GBs in PHt1. Electrostatic forces in a bulk ionic material do not converge as a function of the interatomic distance.

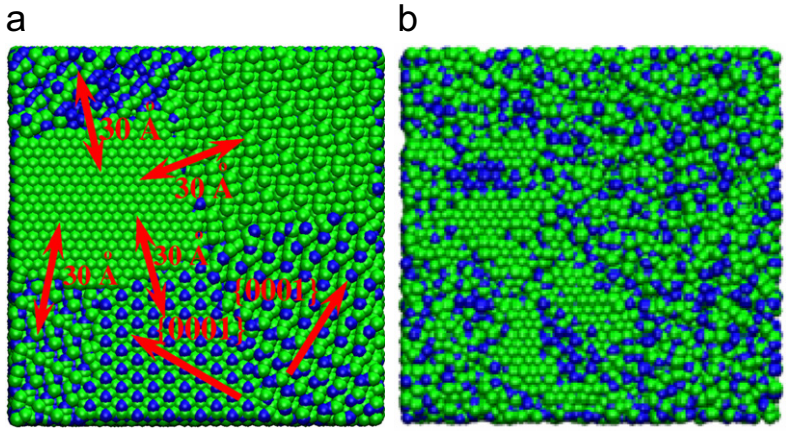


Fig. 7. Mid cross-sections of polycrystalline $Fe_2O_3$ with the average grain size of 7.2 nm (a) before MD equilibration (dark arrows illustrate range of electrostatic forces, white arrows denote the orientation of the {1 0 0 0} crystalline plane in each grain) and (b) after MD equilibration.

However, analyses has shown that beyond a certain cutoff radius interatomic interactions can be neglected (Wolf (1992)). The effective value of the cutoff distance is approximately 30 Å. For smaller distances between charged atoms, the electrostatic forces are very strong. As the distance between charged atoms increases, the force between them diminishes as fast as $\mathbf{r}^{-5}$. Obviously, the effective electrostatic forces from the GBs reach the interior of entire grains when the grain size is of the order of 7.2 nm. This results in strong intergranular interactions between different grains and significant influences of GBs over entire grains. Consequently, the change in structural order is not limited to the GBs but instead can occur over entire grains. We surmise that this is the reason for the significant loss in structural order as shown in Fig. 7(b). However, it is not possible to ascertain whether the structure is still crystalline by visual inspections alone. Possibilities are (1) the complicated primitive unit cell prevents an easy identification of the structural order and (2) amorphization has occurred. Nanocrystalline $Fe_2O_3$ and its composites have been synthesized at the size scales as low as 20 nm, cf. Armelao et al. (1997), Casula et al. (2001), and Cannas et al. (2004). Long et al. (2004) have synthesized $Fe_2O_3$ aerogel structures at the size scale of ~7 nm and observed the appearance of an amorphous $Fe_2O_3$ phase. The diffraction peaks in their analyses show that the $Fe_2O_3$ aerogel mixture has traces of $Fe_3O_4$ (magnetite) and $\gamma$-$Fe_2O_3$ (maghematite) phases. However, the peaks primarily show amorphous characteristics similar to the total $Fe_2O_3$ RDF of equilibrated PHt1 shown later in Fig. 8(b). In order to verify that the final structure is indeed amorphous, partial Fe–Fe, Fe–O, O–O and total $Fe_2O_3$ RDFs for the structure need to be examined. The change in structural order of nanocrystalline $Fe_2O_3$ to amorphous nanophase $Fe_2O_3$ is clear from partial Fe–Fe and total $Fe_2O_3$ RDFs plotted in Fig. 8(a) and (b), respectively. The total $Fe_2O_3$ RDF is calculated by summing up the partial Fe–Fe, Fe–O, and O–O RDFs. Features for the partial Fe–O and O–O RDFs are the same as those for the partial Fe–Fe RDF. As shown in both Fig. 8(a) and (b), the peaks denoting the crystalline order disappear after equilibration, resulting in profiles with amorphous characteristics. Both the partial and the total RDFs indicate a crystalline to amorphous

change in the structural order. It can therefore be concluded that at the simulation lengthscales, the room temperature equilibration of geometrically generated nanocrystalline $Fe_2O_3$ structures results in amorphous $Fe_2O_3$ nanophase structures.

One can question whether the formation of amorphous nanophase $Fe_2O_3$ structures is an artifact of the potential or an actual structural attribute at the lengthscale analyzed. To answer these questions, we use the potential to analyze the equilibration of a single crystal of $Fe_2O_3$ with and without PBCs. Fig. 9(a) and (b) show configurations of a piece of single crystalline $Fe_2O_3$ after equilibration with PBCs and after equilibration with free surfaces, respectively. Obviously, except for possible surface reconstructions in Fig. 9(b), the structural order after equilibration is the same as that before equilibration. This observation suggests that the potential works well for $Fe_2O_3$ single crystals in bulk and in small clusters.

To make sure that amorphous nanophase $Fe_2O_3$ structure formation shown in Fig. 7 is not due to artificially high pressures resulting from the grain structures, the pressures in PHt1, PHt2, and PHt3 during equilibration are compared with that for the single crystals with and without PBCs. The comparison is shown in Fig. 10(a). As shown in the figure, the pressure in nanocrystalline $Fe_2O_3$ is the same as that for single crystal $Fe_2O_3$ with PBCs. Clearly, the potential yields results that are consistent with expected behaviors for both

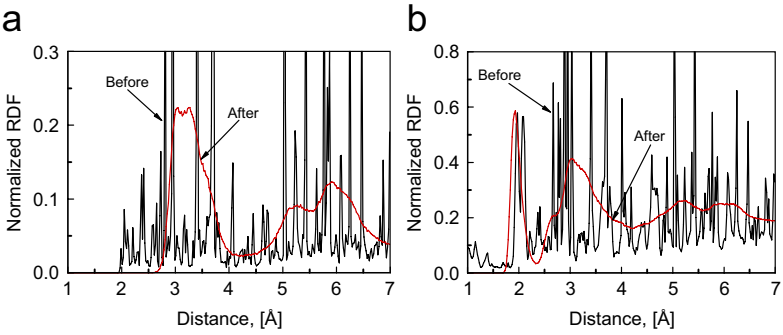


Fig. 8. (a) The Fe–Fe and (b) the total $Fe_2O_3$ RDF for the $Fe_2O_3$ structure with a grain size of 7.2 nm before and after equilibration.

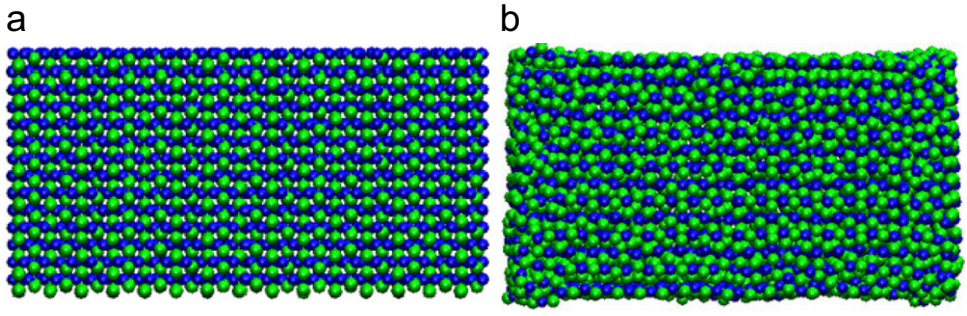


Fig. 9. Single crystal $Fe_2O_3$, (a) after equilibration with periodic boundary conditions and (b) after equilibration as an independent cluster.

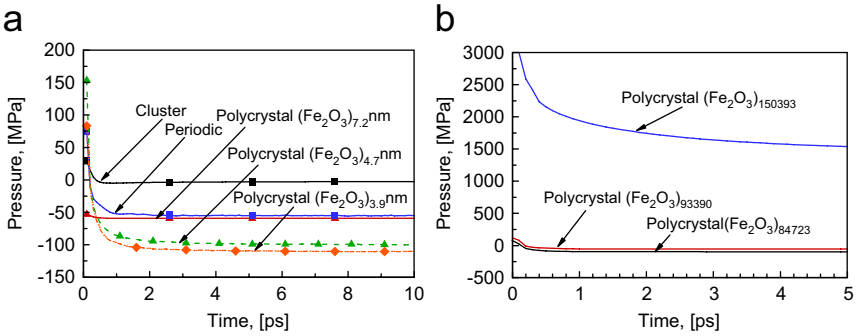


Fig. 10. Time histories of pressure during equilibration (a) for $Fe_2O_3$ structures with different average grain sizes under various conditions and (b) for the $Fe_2O_3$ structure with an average grain size of 7.2 nm and different numbers of atoms along GBs.

single crystalline and nanocrystalline structures. It then can be concluded that amorphization seen in Fig. 7 is not due to artificially high pressures either. To further analyze if the results in Fig. 7 can be caused by unrealistic levels of energy of atoms along GBs that may be very close to each other in the geometrically generated structures of $Fe_2O_3$, the time-histories of pressure during the equilibration of PHt1 with different numbers of atoms along the grain GBs are shown in Fig. 10(b). A relatively high number (150,393) and low number (84,723) are considered along with the number (93,390) considered in the analyses earlier. The decrease in the number of atoms along GBs does not affect the pressure significantly. However, the increase causes the pressure to increase by two orders of magnitude. This result suggests that there is an optimum number of atoms along the GBs in a structure under equilibrium and spacing of GB atoms does not cause any rise in pressure or corresponding change in structural order for the PHt1 structure with 93,390 atoms analyzed earlier.

The $Fe_2O_3$ phase in the $Al+Fe_2O_3$ nanocrystalline composites is also found to have an amorphous structural order after MD equilibration. Consequently, it is not possible to identify the formation and propagation of defects in the $Fe_2O_3$ phase at the length-scale analyzed in this paper. From here on, the defect nucleation and propagation analyses will focus solely on the Al phase. The fraction of atoms in defects and GBs are identified by using a cutoff slip-vector magnitude of 0.25. The same cutoff is also used to identify GBs in Fig. 1(b). The fraction of defect and GB atoms calculated this way may not be a unique indicator of the extent of the change in crystalline order in the composites. However, in combination with strength analyses it serves as an important indicator of the effect of second phases on the strength and deformation of the composites.

## 4. Calculation of tensile strength

In the uniaxial quasistatic deformation analyses of nanocrystalline Cu by Schiøtz et al. (1998), strain was calculated by recording the changes in positions of individual atoms. The average virial stress was calculated at every step in order to obtain the stress–strain relations. A modified version of this approach is used here. An alternative method to obtain uniaxial stress–strain curves is to record strain–time curves at several values of

applied stress and then deduce the stress–strain relations, cf. Van Swygenhoven and Caro (1997). Spearot et al. (2005) have used both methods and found that the modified Schiøtz et al. (1999) method works better because it controls the applied strain and closely emulates controlled displacement experiments. The modifications to the method of Schiøtz et al. (1998) include the use of a combination of the algorithms for NPT and NVT ensembles, cf. Spearot et al. (2005). Alternating steps of stretching and equilibration at constant temperature are carried out to approximate uniaxial quasistatic deformation. Initially, the system is equilibrated at the specified temperature (300 K). During equilibration, NVT equations of motion are used to relax the pressure on the structure in all three directions. During stretching, the computational cell is stretched in the loading direction using a modified version of the NPT equations of motion of Melchionna et al. (1993). The NPT equations ensure that the lateral pressures are relaxed to atmospheric values during the deformation. In this algorithm, the rate of change of a simulation cell volume, $V(t)$, is specified using a barostat friction coefficient parameter $\eta$ such that

$$\frac{\mathrm{d}\eta(t)}{\mathrm{d}t} = \frac{1}{Nk_{\mathrm{B}}T_{\mathrm{ext}}\tau_{\mathrm{P}}^2} V(t)(P - P_{\mathrm{ext}}) \tag{9}$$

and

$$\frac{\mathrm{d}V(t)}{\mathrm{d}t} = 3\eta(t)V(t). \tag{10}$$

Here, $P$ is the instantaneous pressure, $P_{\mathrm{ext}}$ is the externally applied pressure, $N$ is total number of atoms in the system, $k_{\mathrm{B}}$ is the Boltzmann constant, $T_{\mathrm{ext}}$ is the external temperature, and $\tau_{\mathrm{P}}$ is a specified time constant for pressure fluctuations. For a given cross-sectional area, the specification of $\eta$ in Eq. (2) is equivalent to specifying strain rate for the change in simulation cell length. Further, for a given $\eta$, Eq. (1) can be modified as, cf. Spearot et al. (2005),

$$\frac{\mathrm{d}\eta(t)}{\mathrm{d}t} = \frac{1}{Nk_{\mathrm{B}}T_{\mathrm{ext}}\tau_{\mathrm{P}}^2} V(t)(P - P_{\mathrm{ext}}) - \gamma\eta\cdot \tag{11}$$

In the above equation, the term $\eta\gamma$ acts as a damping coefficient for reducing fluctuations in pressure during the stretching of the simulation cell. During the simulations, the system is initially equilibrated at $T_{\mathrm{ext}} = 300\,\mathrm{K}$. After equilibration, the computational cell is stretched in the loading direction using $\eta = 0.1\,\mathrm{ps}^{-1}$. The values of $\gamma = 0.5$ and $P_{\mathrm{ext}} = 1$ atmospheric pressure are used. The values for $\eta$ and $\gamma$ are calculated in trial calculations that focused on achieving the best balance between simulation time (low $\eta$ results in long simulation times and vice-versa) and pressure fluctuations (high $\gamma$ results in excessive pressure damping with increase in residual stresses along periodic boundaries). To choose the right time duration for equilibration between loading steps, trial calculations of the stress–strain curve for a sample nanocrystalline structure are carried out with the equilibration time periods of 0.5, 1.0, 2.0 and 4.0 ps at the same stretching increment period of 0.05 ps. Fluctuations in the stress values are found to be within $\pm 5\%$ of the mean stress values at all strain levels, see Fig. 11. In the analyses reported in the manuscript, the MD equilibration time in between the periods of stretching is chosen as 2.0 ps.

To approximate 3D bulk behavior, PBCs are applied in all directions of the simulation cell. The relatively small number of grains in the simulation cell may cause the calculated behavior to be anisotropic. Van Swygenhoven and Caro (1998) calculated the elastic and

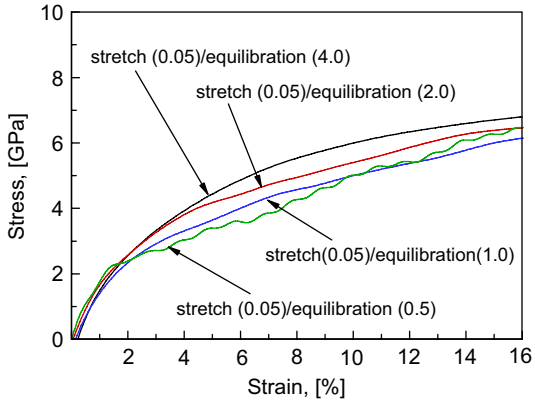


Fig. 11. The dependence of stress–strain relations on load increment and equilibration time.

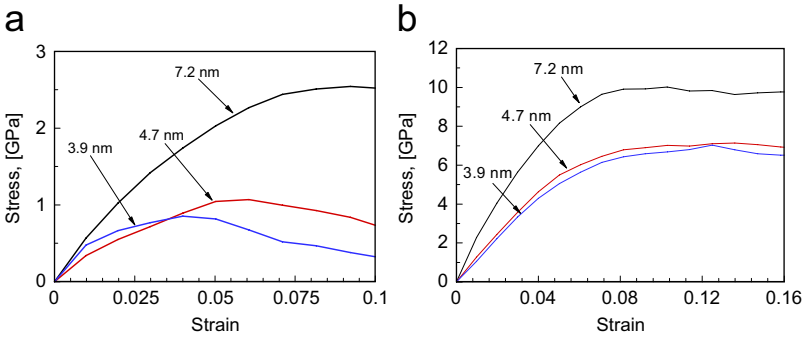


Fig. 12. Tensile stress–strain curves for (a) nanocrystalline Al with different grain sizes and (b) nanophase $Fe_2O_3$ with different grain sizes.

plastic properties along three cubic axes of nanocrystalline structures generated by Voronoi tessellation. They concluded that the fluctuations in the stress–strain responses are not significant. Based on their results, anisotropy is assumed to be insignificant and is not analyzed here. Stress calculation follows the formulation of Zhou (2003) and Zhou and McDowell (2002). The stress in this formulation is calculated over current volume. Therefore, it corresponds to true stress. The strain is calculated based on the change in the current volume of the periodic simulation cell and therefore corresponds to true strain. Due to the non-linear nature of the stress–strain curve, the calculation of the Young's modulus necessitates a compromise between having enough data points for a reliable fit and staying within the initial linear region. It is found that a reasonable compromise is to use the first four data points within a strain of 1% for all material systems. Each data point corresponds to a change in the simulation cell length of 0.25 Å (the cell length is 100 Å). The strain level of 1% is higher than the traditional strain level for defining yielding (0.2%). This perhaps results in a slight underestimate of the Young's modulus. The onset of plastic deformation defines the yield stress $\sigma_y$ which is traditionally taken as the stress where the plastic part of the total strain is 0.002. In the simulations presented in this paper,

the stress continues to increase after the yield point, until it reaches a plateau (the flow stress) and becomes constant or begins to decrease slightly. Typical strain levels during uniaxial deformation are 15–20%. Since $\sigma_y$ is calculated at much lower strain values, we feel that the use of the flow stress to represent the strength of nanocrystalline structures would be more appropriate. The flow stress in this research is calculated as the average stress in the region on the stress–strain curve where stress reaches a maximum. Schiøtz et al. (1999) and Schiøtz and Jacobsen (2003) also calculated the flow stress by averaging the stress values at three arbitrary points in the strain interval of 7–10%.

## 5. Behavior of Al and $Fe_2O_3$

Fig. 12(a) shows the stress–strain curves for PAl1, PAl2, and PAl3 in tension. The values of Young's modulus are 57.7 GPa for PAl1, 33.9 GPa for PAl2, and 48.4 GPa for PAl3. The flow stress is taken as the average of the stress values at strain levels of 4, 6, and 8%. These strain levels are chosen because the stress in at least one of the structures either becomes constant or reaches a maximum at one of these strain values. We note that similar strain levels have been used by other researchers, cf. e.g., Schiøtz et al. (1999) and Lu et al. (2001). The flow strength is found to be 2.5 GPa for PAl1, 0.98 GPa for PAl2, and 0.74 GPa for PAl3. Overall, a softening trend in strength is observed as the average grain size decreases. One exception exists in the Young's modulus value of PAl3 which is higher than that of PAl2. Similar anomalies in stress–strain relations have been observed in the work of Schiøtz and Jacobsen (2003) on nanocrystalline Cu. This behavior can be explained by accounting for the role of GBs in the deformation. At the length scale of analyses, sliding of grains along GBs is the primary mechanism of deformation (see Introduction). Dislocation activity is minimal at this length scale. The total GB surface area increases as the grain size decreases, resulting in softening of the structures. When the size scales are similar for two structures, the difference in the fractions of GBs with high-angle mismatches and the difference in the fractions of atoms in defects and GBs play an important role. The higher fractions of defect atoms and high-angle mismatch GBs in PAl3 as compared to those in PAl2, see Fig. 4(b), pose enhanced constraint on the movement of atoms in PAl3 during initial stretching. The atoms locked in high-angle GBs resist initial tensile deformation, making PAl3 initially stronger than PAl2. However, after significant deformation, the flow is mainly governed by GB sliding which is dominant in PAl3. Because of the increased elongation, GB atoms have stronger mobility in PAl3 than in PAl2 during later stages of deformation. Accordingly, PAl3 has a lower flow strength value than PAl2.

The Young's modulus for these structures varies from 33.9 to 57.7 GPa and increases with grain size. These values are smaller than the value of 70 GPa for single crystalline Al. Similarly, values ranging from 90 to 105 GPa are seen in nanocrystalline Cu, compared with the value of 124 GPa for bulk Cu, cf. Gschneidner (1964). As explained earlier, the primary reason behind this trend is that the atoms in GBs cause the Young's modulus to decrease. A similar observation is made in simulations where the nanocrystalline metal is grown from a molten phase, cf. Phillpot et al. (1995). In our research, plastic yielding occurs at stress values of ~0.5–1.5 GPa in the structures analyzed. It is illustrative to note that, the theoretical shear strength of single crystalline Al ($Gb/2\pi d$) is ~3 GPa.

Fig. 12(b) shows the stress–strain curves for the three $Fe_2O_3$ structures with different grain sizes (PHt1, PHt2, and PHt3 in Fig. 2). The Young's modulus values are 174, 115,

and 107 GPa, respectively. Ductility at all grain sizes is found to be higher than that for Al. Accordingly, the flow strength is evaluated at strain levels of 10%, 12%, and 14%. The flow strength is 9.88, 6.98, and 6.7 GPa for PHt1, PHt2, and PHt3, respectively. Overall, the Young's modulus and flow strength values decrease, as grain size decreases. The tensile strength values observed here are much higher than what is observed in experiments for samples with larger grain sizes, cf. Thadhani (2005). In experiments, specimens with large grain sizes (of the order of microns) show significant fragmentation, resulting in low tensile strength values. Microstructural examinations show that lack of strong cohesion among $Fe_2O_3$ grains is the primary cause for the low strength values. However, experiments have shown that there is a possibility of a high degree of mixing in nanocrystalline $Fe_2O_3$ such that $Fe_2O_3$ grains can have enhanced cohesion, cf. Long et al. (2004) and Cannas et al. (2004). The $Fe_2O_3$ nanostructures analyzed here have similar characteristics, with a high degree of mixing and high inter-grain cohesive strengths which can lead to high tensile strength values. The results in Fig. 12(b) suggest a reverse H–P relation for $Fe_2O_3$. The Young's modulus and the flow strength values are consistently higher than those for Al given earlier. The Young's modulus values of 174, 115, and 107 GPa are lower than the 235 GPa for bulk $Fe_2O_3$, consistent with what is observed for Al. The flow strength values are one order of magnitude higher than the corresponding macrocrystalline values for both $Fe_2O_3$ and Al. The primary factor responsible is the difference between the deformation mechanisms operative at the two length scales. At the macroscale, dislocation motion dominates the deformation process. At the nanoscale, GB sliding dominates the deformation process.

Fig. 13 shows the deformed configurations of the three Al structures and three NCP64 structures at a strain level of 7.5% at the same cross-sections as those shown in Fig. 4. The load is applied in the vertical direction in the cross-section shown. The Al atoms are colored using the slip-vector method. When viewed along the cross-section, it is possible to make a clear distinction between the motion of atoms along defects and GBs in all structures. In addition, it is observed that the qualitative features related to dislocation emission and the motion of atoms along GBs are the same for all arbitrarily chosen cross-sections. Here, the same cross-section is chosen for all structures and this choice indeed gives representative views of the deformation processes. A comparison of Fig. 13(a) and (b) reveals that there is an increase in the number of Al atoms associated with defects due to the presence of the $Fe_2O_3$ phase. The images show that atomic motion associated with the Al phase takes place primarily along the Al–$Fe_2O_3$ interfaces. As pointed out earlier, the $Fe_2O_3$ phase in the composites is amorphous. Correspondingly, the identification of structural defects in the $Fe_2O_3$ phase can not be carried out. Defect analyses here solely concern the Al phase. For the same reason and for clarity, only Al grains are shown in the plots to come for the composites. Grain coarsening is observed at strains above 25%. However, the discussions here are limited to mechanisms at strains up to 15%. Therefore, grain coarsening is not of particular concern.

Fig. 14 shows the deformed configurations of a cross-section at strain levels of 2.5, 5, and 7.5 for each of the three Al structures. These strain levels correspond to the following stages of deformation:

(1) strain hardening (strain of 2.5%);
(2) attainment of maximum stress (strain of 5% ); and
(3) severe plastic deformation (strain of 7.5%).

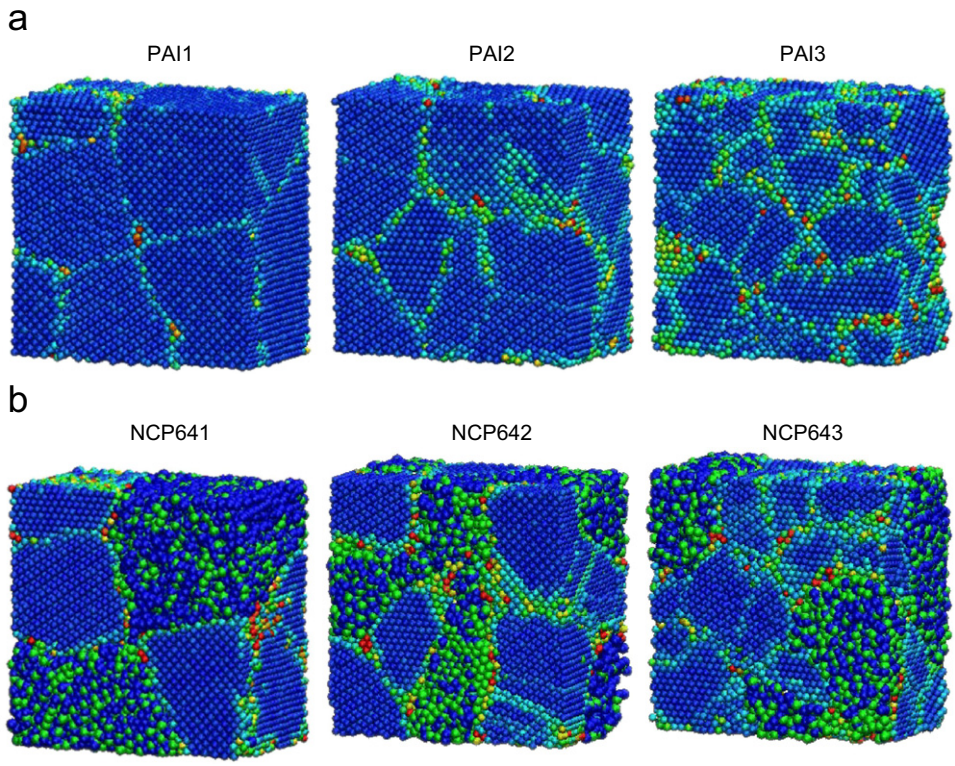


Fig. 13. (a) Deformed configurations of Al structures at a strain level of 7.5%; (b) deformed configurations of the 60%Al + 40%$Fe_2O_3$ composite at a strain of 7.5% (Al atoms are colored using the slip-vector approach; Fe and O atoms are bigger than Al atoms and are colored blue and green, respectively).

Strain hardening is evident in Fig. 12(a). A particular section of the 3D Voronoi tessellated nanocrystalline samples is shown in Figs. 13 and 14 to facilitate a visual comparison of the differences in defect formation across different samples analyzed. Although only a particular section of the samples is shown here, visual observations in 3D indeed reveal a pile-up of dislocations as strain increases. A large number of pile-ups is not seen here primarily because the average grain sizes are relatively small compared with what is analyzed by Van Swygenhoven et al. (2006) and Yamakov et al. (2004). A combination of grain rotation, dislocation pile-up, and twinning contributes to the strain hardening seen in the stress-strain curves.

Fig. 14 shows that the thickening of high-angle GBs as strain increases is more pronounced than that of low-angle GBs. This indicates that atoms in high-angle GBs have a higher level of mobility. As deformation proceeds, atoms move into GBs, resulting in larger thicknesses of the GBs. The lower mobility of low-angle GBs is primarily due to the smaller orientation difference of the neighboring grains. Using a 2D model, Fang et al. (2004) found that dislocation emission in Ni occurs earlier when Ni single crystals are stacked along low-angle GBs than when they are stacked along high-angle GBs. Indeed, it would make sense that low-angle GBs consist of a series of misfit-type dislocations that may well serve as sources for nucleation of dislocations during deformation. Their finding

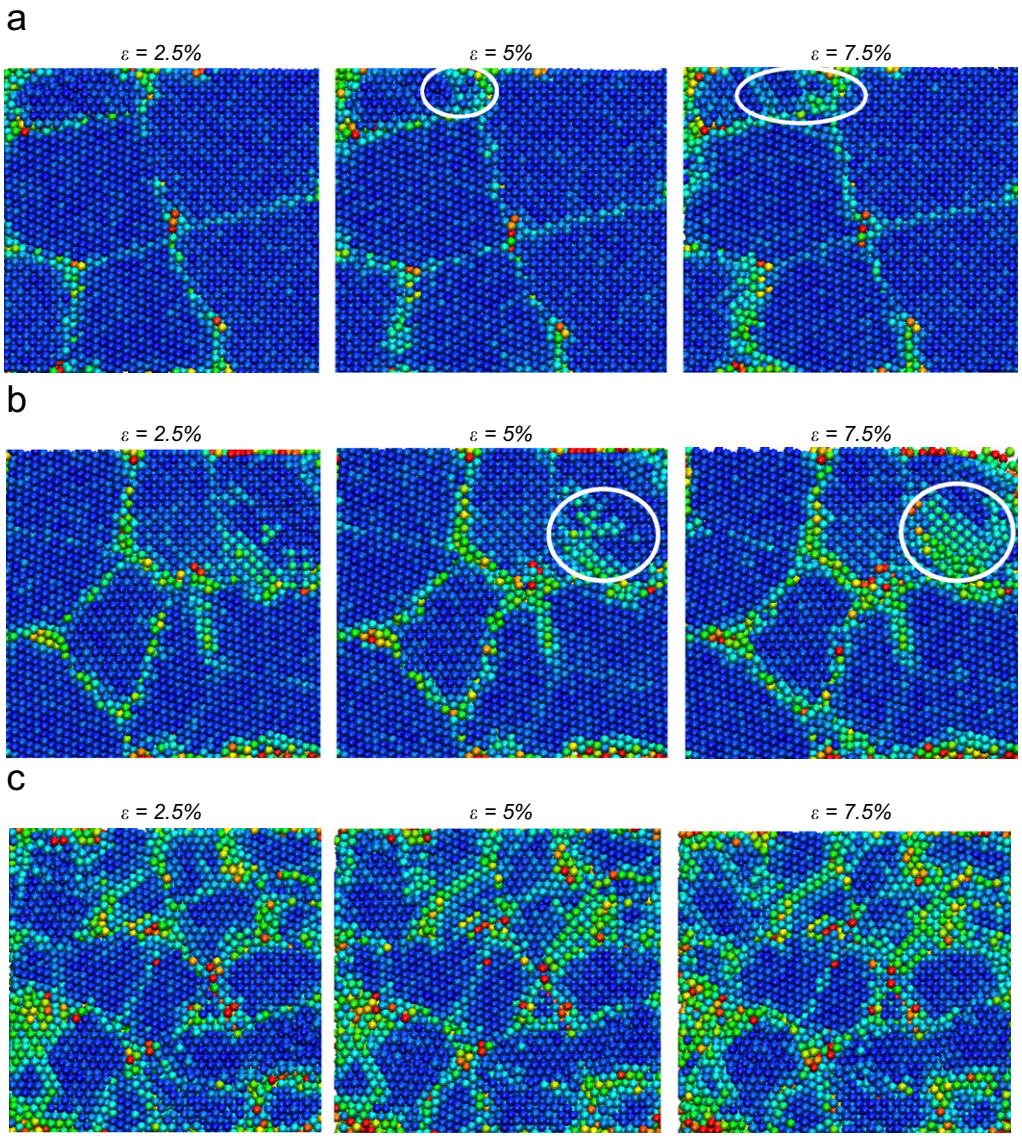


Fig. 14. Deformed cross-sections of Al structures with grain sizes of (a) 7.2 nm (PAl1), (b) 4.7 nm (PAl2), and (c) 3.9 nm (PAl3) (the circles highlight stacking faults, loading is parallel to the plane of view and in the horizontal direction).

is in contrast to our observation that most dislocation emissions originate from high-angle GBs. We note that their nanostructures have only one type of GB stacked in an array along an axis. In the current work, low-angle and high-angle GBs are present in nearly the same proportion.

We surmise that when low-angle and high-angle boundaries are present simultaneously, a major portion of the applied load is transferred to the high-angle GBs. Since atoms in

high-angle GBs have higher mobility compared with atoms in low-angle GBs, dislocation emission is more likely to occur earlier from high-angle GBs as deformation progresses. Dislocations are emitted from high-angle GBs that are both parallel and perpendicular to the loading axis. Using a 2D model, Yamakov et al. (2002a) observed twinning in Al grains in the size range of 30–90 nm. Twinning is not observed in our 3D model at small strains because the deformation occurs predominantly through the movement of atoms along GBs. At larger strains, dislocations emitted from GBs in some of the structures analyzed form stacking faults that ultimately lead to twinning in the Al grains. Van Swygenhoven et al. (2004) have analyzed the formation and annihilation of partial and full dislocations in nanocrystalline Al. The focus of their analyses is on obtaining a correlation between the values of single crystalline stable and unstable stacking faults and the corresponding emission of partial or full/unit dislocations. Emission of unit dislocations instead of partial dislocations in nanocrystalline Al has been observed using the potential used in the current research, cf. Tomar and Zhou (2006a), in agreement with the findings of Van Swygenhoven et al. (2004).

In PAl1 and PAl2, dislocation emission occurs in later stages of deformation and stacking faults begin to appear at a strain of 5%. When the strain reaches 7.5%, the width of the stacking fault band is of the order of the corresponding grain size. The emission in PAl1 is from a $\{1\,1\,0\}$–$\{1\,1\,1\}$ high-angle GB at a strain of 5% and from $\{1\,1\,0\}$–$\{1\,1\,1\}$ and $\{1\,1\,1\}$–$\{1\,0\,0\}$ high-angle GBs at a strain of 7.5%. No dislocation emission is observed from low-angle GBs. The emission in PAl2 starts from a $\{1\,1\,1\}$–$\{1\,0\,0\}$ high-angle GB when the strain reaches 5%. At a strain of 7.5%, the stacking fault behind the emitted dislocation has reached a low-angle $\{1\,0\,0\}$–$\{1\,0\,0\}$ GB, see Fig. 14(b). Significant thickening of the GBs occurs in PAl3 without dislocation emission at any stage of deformation. In addition, the thicknesses of the GBs are higher than those in PAl1 and PAl2. The thickness of some of the GBs in PAl3 is on the order of the corresponding grain size. When such GBs share a junction or when they are close to each other, the initial movements of atoms in these GBs interlock, causing the Young's modulus value of PAl3 to be higher than that for PAl2, see (Fig. 12(a)).

Overall, the picture that emerges from the analyses is that plastic deformation occurs primarily through a large number of sliding events along GBs, with only a minor contribution from dislocation motion inside grains. Occasionally, a partial dislocation is nucleated at a GB and moves through the grain. Dislocation motion is responsible for a minor part of the total deformation. The softening at small grain sizes is, therefore, due to the larger fractions of atoms at GBs. This deformation mode is in some ways similar to the manner in which GBs carry most of the deformation in superplasticity. However, superplastic deformation through GB sliding occurs at high temperatures. Here, the deformation occurs at room temperature and is driven by high stresses on GBs. To further understand the deformation mechanisms, the fractions of atoms in defects are calculated at different levels of strain, as shown in Fig. 15. Here, defect atoms are defined as those having a slip-vector magnitude of more than 0.25. Using the same classifications, GBs are shown separately from bulk nanocrystalline grains in Fig. 1(b). The changes in the fraction of defect atoms in all structures are non-linearly related to increases in deformation. The initial increase in the fraction of defect atoms as a function of the deformation level is very small. At large strains the increase is up to three times than that at smaller strains. This is in accordance with the earlier explanations of the deformation mechanism. Initially, sliding along GBs dominates the deformation process. Later on, dislocation emission adds to the

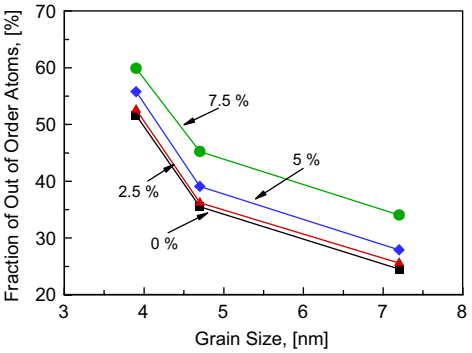


Fig. 15. The fraction of defect atoms as a function of grain size at different levels of strain in nanocrystalline Al.

increase in the fraction of defect atoms. The increase in the fraction of defect atoms is the highest in PAl1.

The results presented so far show that, in a majority of cases, plastic deformation takes place by means of GB sliding. The sliding is associated with the lower elastic moduli of disordered GBs which are elastically more compliant than grain interiors. Experimental data on the variation in strength of nanocrystalline Al with average grain size is not available. However, nanocrystalline Al has been prepared in laboratory using nanoparticle consolidation and severe plastic deformation procedures, cf. Tjong and Chen (2004). In this respect, it is important to point out that the results on Al in terms of both strength and Young's modulus are consistent with experimental observations for nanocrystalline *fcc* Cu, cf. Gschneidner (1964).

## 6. Behavior of $Al + Fe_2O_3$ composites

Fig. 16 shows the stress-strain curves for $40\%Al + 60\%Fe_2O_3$ (NCP46) and $60\%Al + 40\%Fe_2O_3$ (NCP64) composites. The Young's modulus values for NCP461, NCP462, and NCP463 are 151.6, 66.0, and 52.3 GPa, respectively. The Young's modulus values for NCP641, NCP642, and NCP643 are 127.6, 63.24, and 51.2 GPa, respectively. The flow strength is evaluated at strain levels of 10%, 12% and 14%. The values are 7.56, 4.05, and 2.72 GPa for NCP461, NCP462, and NCP463, respectively. For NCP641, NCP642, and NCP643 the values are 5.62, 3.11, and 2.42 GPa, respectively. Overall, as the average grain size increases, both the strength and the Young's modulus increase. The tensile strengths for the composites lie between those for Al and $Fe_2O_3$ given earlier. The deformation curves show strain-hardening ending at ~7.5% strain. At all grain sizes, NCP46 has higher compressive and tensile strengths than NCP64. Obviously, at the same grain size, the structure with the lower volume fraction of Al is stronger than the structure with the higher volume fraction of Al. The strength of the composites increases with the volume fraction of $Fe_2O_3$. Clearly, electrostatic forces in the $Fe_2O_3$ phase strongly affect the mechanical strength of the composites.

Fig. 17 shows the Al phase in NCP46 and NCP64 at a strain of 7.5%. The atoms are colored using the slip-vector approach. At this strain, sufficient deformation has occurred in all structures therefore an easy comparison can be made. The cross-sections shown here are the same as those in Fig. 14, facilitating a direct comparison between the composites

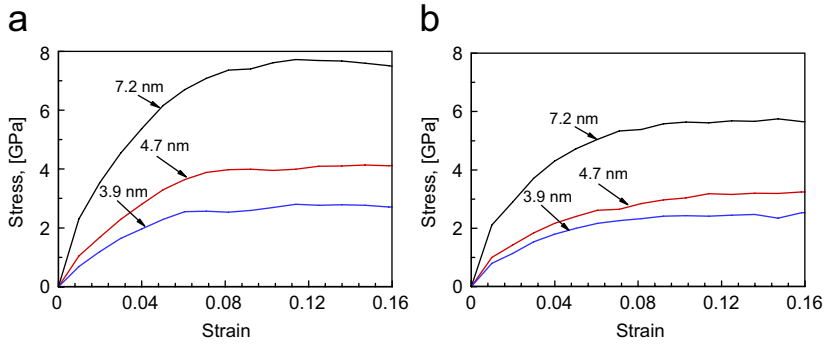


Fig. 16. Stress–strain curves for (a) 40%Al + 60%$Fe_2O_3$ and (b) 60%Al + 40%$Fe_2O_3$ with different grain sizes.

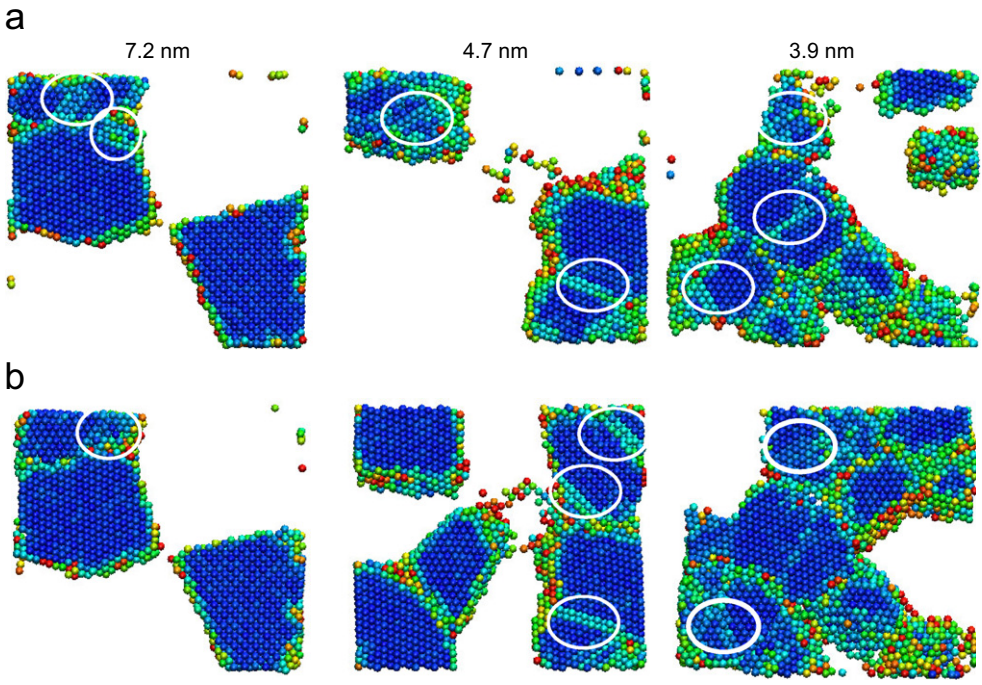


Fig. 17. Deformed configurations of Al grains in (a) 40%Al + 60%$Fe_2O_3$ and (b) 60%Al + 40%$Fe_2O_3$ composites at a strain of 7.5% (Cross-sections shown are the same as those in Fig. 14, the circles highlight stacking faults).

and the Al structures. Note that the Al grains in both Figs. 14 and 17 have the same size, shape and initial locations in their respective structures. Fig. 17 shows that NCP46 has a higher level of dislocation emission than NCP64. This is due to higher interfacial stresses in NCP46 caused by the higher volume fraction of the $Fe_2O_3$ phase. At any particular grain size, there is a higher level of dislocation activity in the composites than in the Al structures. This indicates that the presence of the $Fe_2O_3$ phase induces higher stresses that have both short and long-range effects which cause enhanced GB activities and dislocation

emission. The increased interfacial activity at the GBs of the Al grains in the composites relative to the activity at the GBs of the grains in the Al structures causes an increase in strength which in turn enhances the emission of dislocations. Consistent with this observation is the fact that the thickness of the Al layer at the Al and $Fe_2O_3$ interfaces in all composites is higher than the thickness of corresponding GBs in the nanocrystalline Al structures. These observations indicate that a similar mechanism of deformation is operative in the composites, in the nanocrystalline Al and in the $Fe_2O_3$ phase. This mechanism is GB sliding under strong electrostatic forces. It is also noted that the stress at the Al–$Fe_2O_3$ interfaces causes the dislocation emission through the high-angle as well as the low-angle GBs. This observation emphasizes different roles played by the Al–$Fe_2O_3$ interface atoms and the Al and $Fe_2O_3$ GB atoms in the deformation.

To further understand the deformation mechanism, the fraction of Al atoms in defects and GBs as a function of grain size and strain level is shown in Fig. 18. The fractions are calculated using the method established earlier, see Fig. 1(b). The result is compared with that in Fig. 15. In the composites, the rate of increase in the fraction of Al atoms in defects and GBs as a function of strain is higher for structures with smaller grain sizes. On the other hand, in nanocrystalline Al (Fig. 15) the rate of increase is higher in structures with larger grain sizes. This is natural since in composites with smaller grain sizes, a larger fraction of Al atoms are involved in interfaces with $Fe_2O_3$. As pointed out earlier, interfaces of $Fe_2O_3$ with Al have higher fractions of Al atoms in defects and GBs. Consequently, smaller grain sizes and higher interfacial areas cause increases in the fraction of Al atoms in defects and GBs as a function of strain. The fraction of Al atoms in defects and GBs in NCP46 is found to be higher than that in NCP64 at all grain sizes. This is consistent with the effect of higher stresses at Al–$Fe_2O_3$ interfaces on the fraction of Al atoms in defects and GBs. Obviously, the presence of the $Fe_2O_3$ phase enhances defect formation in the Al phase which carries higher levels of stresses than it would have without the harder $Fe_2O_3$ phase.

The challenges in identifying structural defects in the amorphous $Fe_2O_3$ phase aside, the fact that $Fe_2O_3$ is a much stronger phase than Al dictates that most deformation in the composites occurs in the Al phase and among the Al/$Fe_2O_3$ GBs. Fig. 12 shows that the flow strength of $Fe_2O_3$ is 3–4 times that of Al. Indeed, there is very little deformation in $Fe_2O_3$, as demonstrated by Figs. 19 and 20 which show, respectively, the RDFs before

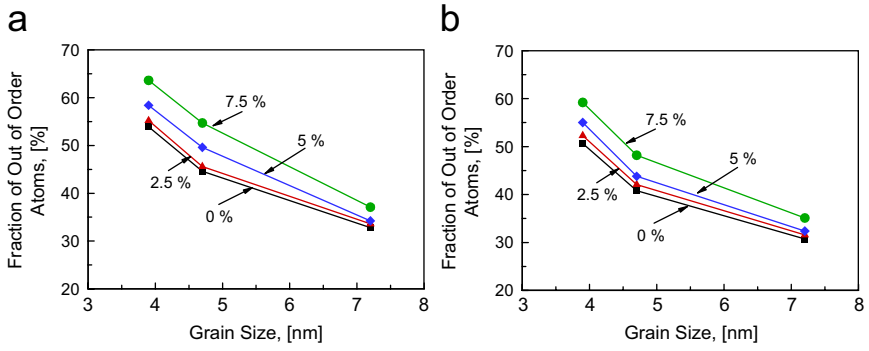


Fig. 18. The fraction of Al atoms associated with defects and GBs as a function of grain size at different values of tensile strain in (a) 40%Al + 60%$Fe_2O_3$ and (b) 60%Al + 40%$Fe_2O_3$.

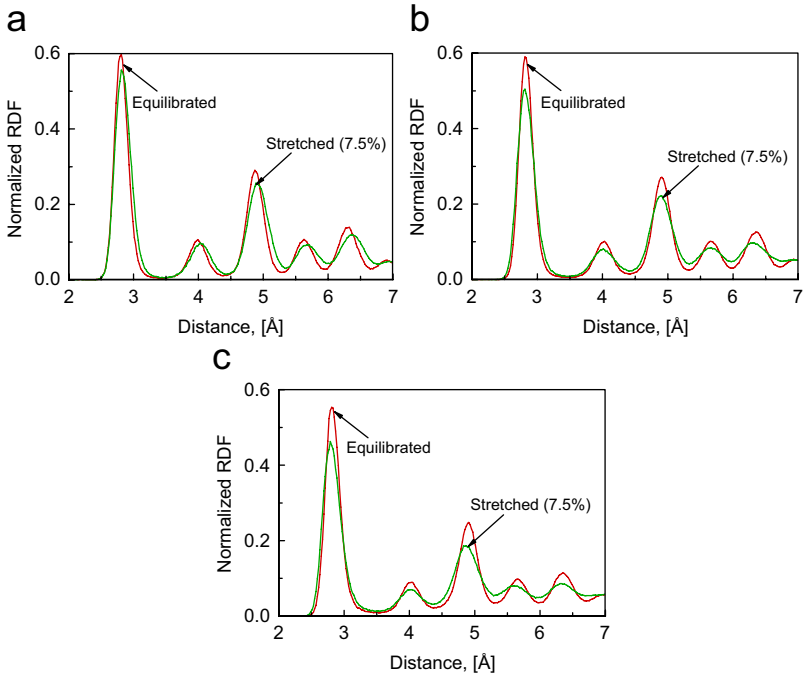


Fig. 19. Partial Al–Al RDFs before deformation and after a tensile deformation of 7.5% for NCP64 structures with grain sizes of (a) 7.2 nm, (b) 4.7 nm, and (c) 3.9 nm.

deformation and after a deformation of 7.5% for Al and $Fe_2O_3$ in NCP64. While the partial Al–Al RDFs in Fig. 19 show significant deformation associated with Al, the total $Fe_2O_3$ RDFs in Fig. 20 show very little deformation in $Fe_2O_3$.

## 7. Hall–Petch relations as a function of phase volume fraction

Fig. 21 shows the Young's moduli and the flow strengths in tension for all material samples analyzed as functions of the average grain size. In both figures, the H–P relationships show a clear dependence on the volume fractions of Al and $Fe_2O_3$. For the composite structures, the H–P relationships lie between those of PAl and PHt. However, the relationships for the composites cannot be simply obtained from the relationships for PAl and PHt based on the rule of mixture. This is primarily because the deformation in the composites is strongly affected by the Al–$Fe_2O_3$ interfaces. Depending on the relative orientations of the two phases at an interface, the contribution of the interface to the strength of a composite varies. As shown earlier during the analyses on the nanocomposites, the interface has a stronger effect in structures with smaller average grain sizes than in structures with larger average grain sizes because of the larger interfacial areas at smaller grain sizes. Consequently, for larger average grain sizes the strength of the composites might be more accurately estimated based on the volume fractions of the individual phases. This is clear from the results for the 7.2 nm structures. Specifically, the strength for these structures can be more closely obtained from those of the pure Al

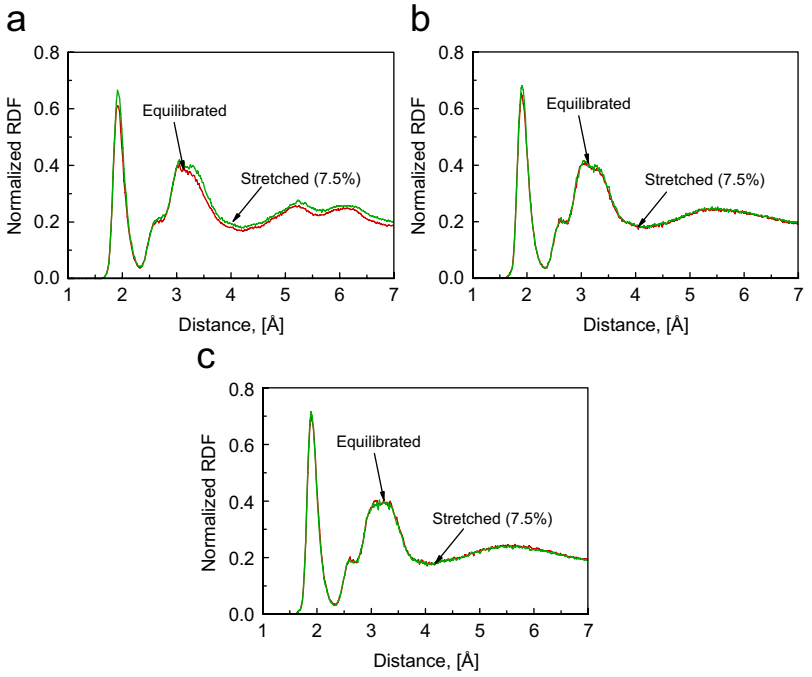


Fig. 20. Total $Fe_2O_3$ RDFs before deformation and after a tensile deformation of 7.5% for NCP64 structures with grain sizes of (a) 7.2 nm, (b) 4.7 nm, and (c) 3.9 nm.

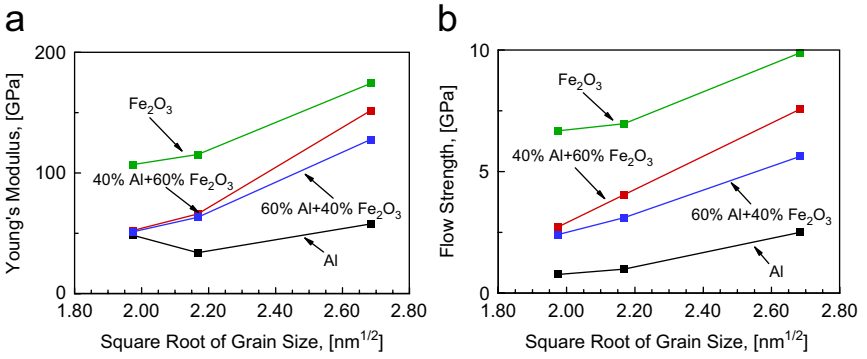


Fig. 21. The dependence on grain size of (a) the Young's modulus and (b) the flow strength at different phase volume fractions.

phase and pure $Fe_2O_3$ phase using the rule of mixture. This, however, cannot be carried out for the structures with average grain sizes of 4.7 and 3.9 nm. At these grain sizes, there is a non-proportional increase in the defect and interfacial atoms. Consequently, the interfacial and GB atoms have larger contributions to the calculated strength values. This result points out that it may be possible for nanocomposite structures to have a critical

grain size above which the strength of a nanocomposite can be calculated using the rule of mixture. Below the critical grain size, the large volume of interfacial atoms in the composites causes the rule of mixture to be ineffective. The GB mismatch and the interfacial stresses also need to be considered to form an appropriate relation, especially at smaller grain sizes. The effects of GBs and interfaces diminish as the average grain size increases. For nanocrystalline structures with grain sizes in the domain where dislocations contribute significantly to the deformation mechanism, it should be possible to neglect the effects associated with GB mismatches and interfacial stresses.

Another important observation from Fig. 21 is that the strength–grain size relations are strongly dependent on the volume fraction of $Fe_2O_3$. Structures with higher volume fractions of $Fe_2O_3$ have steeper slopes in Fig. 21. This indicates that electrostatic forces enhance GB sliding in structures with smaller grain sizes. In both plots, the relationship between the strength and the square root of the grain size for nanocrystalline Al is not linear. This is because high-angle GBs play different roles in PAl2 and PAl3. As pointed earlier, the difference in the average grain sizes for PAl2 and PAl3 is very small. However, there is a big difference in the fraction of defect and GB atoms and in the arrangement of the low-angle and high-angle GBs. At the nanoscale grain sizes, interfaces and GBs dominate the deformation mechanism. Accordingly, the strength of a nanocrystalline structure is a function of the arrangement of GBs (low-angle vs. high-angle) and interfaces in addition to the average grain size. Difference in the arrangement of GBs precludes a linear strength and the square root of average grain size relationship. Similar trends in the H–P relationship are reported by Schiøtz et al. (1998) for nanocrystalline Cu, by Liao et al. (2004) for nanocrystalline Ni and by El-Sherik et al. (1992) through experiments on electroplated Ni samples. In all the cases, the Young's modulus values are lower than those found for the corresponding macrocrystalline values. The flow strength values for the pure phases approach the ideal shear strengths of the corresponding single crystalline systems.

## 8. Summary and conclusions

The quasistatic tensile deformation behavior of nanocrystalline Al, $Fe_2O_3$, and $Al + Fe_2O_3$ composites with average grain sizes between 3.9 and 7.2 nm has been analyzed. The following conclusions summarize the results of the analyses.

(1) In all structures analyzed, the Young's modulus is lower than that for the corresponding macrocrystalline material. The flow strengths of pure Al and pure $Fe_2O_3$ structures approach the ideal shear strengths of their corresponding single crystals. (Section 5, first two paragraphs).
(2) In all the nanocrystalline structures, the underlying mechanism of deformation is GB sliding assisted by electrostatic forces along the Al–$Fe_2O_3$ interfaces. Dislocation emission in the Al phase plays a secondary role. In the case of nanocrystalline Al, the extent of GB sliding is dictated by the fraction of high-angle GBs which to a large extent determine the strength level of a nanostructure. (Figs. 14, 15, 17, and 18)
(3) Dislocation emission primarily initiates from high-angle GBs whose effect on strength is most pronounced at smaller grain sizes with corresponding fractions of GB atoms approaching 50%. The effect of GB mismatch on strength diminishes as the average grain size increases. The dislocation activities in the Al phase of the composites are at an enhanced level compared with those in pure nanocrystalline Al, partly due to the

higher interfacial stresses induced by the stronger $Fe_2O_3$ phase in the composites. In pure Al, dislocation emission occurs primarily along high-angle GBs. In the composites, however, dislocation emission occurs from both high-angle and the low-angle GBs. This may be because of the electrostatic forces at the Al–$Fe_2O_3$ interfaces in the composites. The fraction of defect atoms in the Al phase increases as the volume fraction of the $Fe_2O_3$ phase increases. (Figs. 14, 15, 17, and 18)

(4) Reverse Hall–Petch relations are observed for all the Al, $Fe_2O_3$, and Al + $Fe_2O_3$ nanostructures analyzed. This phenomenon is associated with the sliding of grains along GBs. For $Fe_2O_3$, the relation is linear. This can be attributed to denser packing of atoms in nanocrystalline $Fe_2O_3$ because of its amorphous structural order. As the volume fraction of the $Fe_2O_3$ phase decreases, nonlinearity in the reverse H–P relation arises. For nanocrystalline Al, the strength-square root of grain size relationship is nonlinear because of the strong structural order effects at smaller grain sizes due to the presence of both high-angle and low-angle GBs. (Fig. 21)

(5) In general, the strength of an Al + $Fe_2O_3$ nanocomposite cannot be obtained from the strengths of the Al and $Fe_2O_3$ nanostructures of the same grain size using the rule of mixture. The strength of the composite is strongly affected by interfaces between the phases. This influence is the strongest at small grain sizes and diminishes as the grain size increases. For composites with grain sizes above the critical value, the observed dependence of strength on volume fraction is in agreement with experimental observations. This points to the possibility that the strength of the nanocomposites can only be calculated using the mixture theory if the average grain size is above a critical value. Below the critical grain size, an accurate account of interfacial stresses is important for the prediction of the strength. For structures with grain sizes for which dislocations contribute significantly to the overall deformation, it is possible to neglect the effects of GB mismatches and interfacial stresses. (Section 7)

The observations reported here provide important data and insights for formulating continuum relations for multi-component materials with nanosize grains.

## Acknowledgment

Support from an AFOSR MURI on Multifunctional Energetic Structural Materials at Georgia Tech is gratefully acknowledged. Vikas Tomar gratefully acknowledges the startup support from the University of Notre Dame. Computations are carried out at the NAVO, ERDC, and AHPCRC MSRCs. The authors thank Prof. Julian Gale for providing the molecular statics code GULP 1.3 and Prof. Will Smith for providing DL_POLY2.14 which are modified and used in the current research.

## References

Abraham, F.F., 2003. How fast can cracks move? A research adventure in materials failure using millions of atoms and big computers. Adv. Phys. 52 (8), 727–790.

Armelao, L., Armigliato, A., Bozio, R., Colombo, P., 1997. Sol–gel processing of nanocrystalline hematite thin films. J. Mater. Res. 12 (6), 1441–1444.

Born, M., Huang, K., 1954. Dynamical Theory of Crystal Lattices. Clarendon Press, Oxford.

Buehler, M.J., 2006. Dynamical fracture instabilities due to local hyperelasticity at crack tips. Nature 439 (19), 307–310.

Buehler, M.J., Hartmaier, A., Gao, H., Duchaineau, M., Abraham, F.F., 2004. Atomic plasticity: description and analysis of a one-billion atom simulation of ductile materials failure. Comput. Meth. Appl. Mech. Eng. 193, 5257–5282.

Cannas, C., Musinu, A., Navarra, G., Piccaluga, G., 2004. Structural investigation of $Fe_2O_3$–$SiO_2$ nanocomposites through radial distribution functions analysis. Phys. Chem. Chem. Phys. 6, 3530–3534.

Carlsson, A.E., 1990. Beyond pair potentials in elemental transition metals and semiconductors. Solid State Phys. 43, 1–91.

Casula, M.F., Corrias, A., Paschina, G., 2001. Iron oxide–silica aerogel and xerogel nanocomposite materials. J. Non-Cryst. Solids 293–295, 25–31.

Catlow, C.R.A., Mackrodt, W.C. (Eds.), 1982. Computer Simulation of Solids. Lecture Notes in Physics. Berlin, Springer.

Chen, D., 1995. Structural modeling of nanocrystalline materials. Comput. Mat. Sci. 3 (3), 327–333.

Derlet, P.M., Van Swygenhoven, H., Hasnaoui, A., 2003. Atomistic simulation of dislocation emission in nanosized grain boundaries. Philos. Mag. 83 (31–34), 3569–3575.

El-Sherik, A.M., Erb, U., Palumbo, G., Aust, K.T., 1992. Deviations from hall–petch behaviour in as-prepared nanocrystalline nickel. Scripta Metall. Mater. 27 (9), 1185–1188.

Fang, H., Horstemeyer, M.F., Baskes, M.I., Solanki, K., 2004. Atomisitc simulations of Bauschinger effects of metals with high angle and low angle grain boundaries. Comput. Meth. Appl. Mech. Eng. 193, 1789–1802.

Farkas, D., Mehl, M.J., Papaconstantopoulos, D.A., 2001. Lattice trapping of cracks in Fe using an interatomic potential derived from experimental data and *ab initio* calculations. Mater. Res. Soc. Symp. Proc. 653, Z.6.4.1–Z.6.4.6.

Farkas, D., Willemann, M., Hyde, B., 2005. Atomistic mechanisms of fatigue in nanocrystalline metals. Phys. Rev. Lett. 94, 165502.

Fedorov, A.A., Gutkin, M.Y., Ovid'ko, I.A., 2003. Transformations of grain boundary dislocation pile-ups in nano- and polycrystalline materials. Acta Mater. 51 (4), 887–898.

Gleiter, H., 2000. Nanostructured materials: Basic concepts and microstructure. Acta Mater. 48, 1–29.

Granier, J.J., Pantoya, M.L., 2004. The effect of size distribution on burn rate in nanocomposite thermites: a probability density function study. Combust. Theory Modell. 8, 555–565.

Gross, D., Li, M., 2002. Constructing microstructures of poly- and nanocrystalline materials for numerical modeling and simulation. Appl. Phys. Lett. 80 (5), 746–748.

Gschneidner, K.A., 1964. Physical properties and interrelationships of metallic and semimetallic elements. Solid State Phys. 16, 275–426.

Gutkin, M.Y., Ovid'ko, L.A., Skiba, N.V., 2003. Crossover from grain boundary sliding to rotational deformation in nanocrystalline materials. Acta Mater. 51 (14), 4059–4071.

Hahn, H., Padmanabhan, K.A., 1997. A model for the deformation of nanocrystalline materials. Philos. Mag. B 76, 559–571.

Hahn, H., Mondal, P., Padmanabhan, K.A., 1997. Plastic deformation of nanocrystalline materials. Nanostruct. Mater. 9 (1–8), 603–606.

Haslam, A.J., Phillpot, S.R., Wolf, D., Moldovan, D., Gleiter, H., 2001. Mechanisms of grain growth in nanocrystalline *fcc* metals by molecular-dynamics simulation. Mater. Sci. Eng. A 318, 293–312.

Honeycutt, J.D., Anderson, H.C., 1987. Molecular dynamics study of melting and freezing of small Lennard–Jones clusters. J. Phys. Chem. 91, 4950–4963.

Humphrey, W., Dalke, A., Schulten, K., 1996. VMD—visual molecular dynamics. J. Mol. Graph. 14.1, 33–38.

Huntington, H.B., 1958. The elastic constants of crystals. In: Seitz, F., Turnbull, D. (Eds.), Solid State Physics: Advances in Research and Applications, vol. 7. New York, Academic Press, pp. 213–351.

Kadau, K., Germann, T.C., Lomdahl, P.S., Holian, B.L., 2002. Microscopic view of structural phase transitions induced by shock waves. Science 296, 1681.

Keblinski, P., Wolf, D., Gleiter, H., 1998. Molecular-dynamics simulation of grain-boundary diffusion creep. Interface Sci. 6, 205–212.

Kelchner, C.L., Plimpton, S.J., Hamilton, J.C., 1998. Dislocation nucleation and defect structure during surface indentation. Phys. Rev. B 58 (17), 11085–11088.

Konstantinidis, D.A., Aifantis, E.C., 1998. On the Anomalous hardness of nanocrystalline materials. Nanostruct. Mater. 10 (7), 1111–1118.

Kumar, K.S., Van Swygenhoven, H., Suresh, S., 2003. Mechanical behavior of nanocrystalline metals and alloys. Acta Mater. 51, 5743–5774.

Latapie, A., Farkas, D., 2004. Molecular dynamics investigation of the fracture behavior of nanocrystalline α-Fe. Phys. Rev. B 69, 134110–134118.

Liao, X.Z., Zhou, F., Lavernia, E.J., He, D.W., Zhua, Y.T., 2003a. Deformation twins in nanocrystalline Al. Appl. Phys. Lett. 83 (24), 5062–5064.

Liao, X.Z., Zhou, F., Lavernia, E.J., Srinivasan, S.G., Baskes, M.I., He, D.W., Zhu, Y.T., 2003b. Appl. Phys. Lett. 83, 632.

Liao, X.Z., Srinivasan, S.G., Zhao, Y.H., Baskes, M.I., Zhua, Y.T., Zhou, F., Lavernia, E.J., Xu, H.F., 2004. Formation mechanism of wide stacking faults in nanocrystalline Al. Appl. Phys. Lett. 84 (18), 3564–3566.

Long, J.W., Logan, M.S., Rhodes, C.P., Carpenter, E.E., Stroud, R.M., Rolison, D.R., 2004. Nanocrystalline iron oxide aerogels as mesoporous magnetic architectures. J. Am. Chem. Soc. 126 (51), 16879–16889.

Lu, L., Li, S.X., Lu, K., 2001. An abnormal strain rate effect on tensile behavior in nanocrystalline copper. Scripta Mater. 45 (10), 1163–1169.

Melchionna, S., Ciccotti, G., Holian, B.L., 1993. Hoover NPT dynamics for systems varying in shape and size. Mol. Phys. 78 (3), 533–544.

Ogata, S., Iyetomi, H., Tsuruta, K., Shimojo, F., Nakano, A., Kalia, R.K., Vashishta, P., 2000. Role of atomic charge transfer on sintering of $TiO_2$ nanoparticles: variable charge molecular dynamics. J. Appl. Phys. 88 (10), 6011–6015.

Phillpot, S.R., Wolf, D., Gleiter, H., 1995. Molecular-dynamics study of the synthesis and characterization of a fully dense, three-dimensional nanocrystalline material. J. Appl. Phys. 78 (2), 847–861.

Rodríguez de la Fuente, O., Zimmerman, J.A., González, M.A., Figuera, J.d.l., Hamilton, J.C., Wu Pai, W., Rojo, J.M., 2002. Dislocation emission around nanoindentations on a (0 0 1) *fcc* metal surface studied by scanning tunneling microscopy and atomistic simulations. Phys. Rev. Lett. 88 (3), 036101–036104.

Schiøtz, J., Jacobsen, K.W., 2003. A maximum in the strength of nanocrystalline Cu. Science 301 (5638), 1357–1359.

Schiøtz, J., Di Tolla, F.D., Jacobsen, K.W., 1998. Softening of nanocrystalline metals at very small grain sizes. Nature 391, 561–563.

Schiøtz, J., Vegge, T., Di Tolla, F.D., Jacobsen, K.W., 1999. Atomic-scale simulations of the mechanical deformation of nanocrystalline metals. Phys. Rev. B 60, 11971–11983.

Smith, W., Yong, C.W., Rodger, P.M., 2002. DL_POLY: Application to molecular simulation. Mol. Simul. 28 (5), 385–471.

Spearot, D.E., Jacob, K.I. and McDowell, D.L., 2005. Nucleation of dislocations from [0 0 1] bicrystal Interfaces in aluminum. Acta Mater., in press.

Strietz, F.H., Mintmire, J.W., 1994. Electrostatic potentials for metal-oxide surfaces and interfaces. Phys. Rev. B 50 (16), 11996–12003.

Thadhani, N., 2005. Private communication.

Tillotson, T.M., Gash, A.E., Simpson, R.L., Hrubesh, L.W., Satcher Jr., J.H., Poco, J.F., 2001. Nanostructures energetic materials using sol-gel methodologies. J. Non-Cryst. Solids 285, 338–345.

Tjong, S.C., Chen, H., 2004. Nonocrystalline materials and coatings. Mater. Sci. Eng. R 45, 1–88.

Tomar, V., 2005. Atomistic modeling of the $Al+Fe_2O_3$ material system using classical molecular dynamics. Mechanical Engineering. Atlanta, Georgia Institute of Technology. PhD Thesis, p. 295.

Tomar, V. and Zhou, M., 2004. A molecular dynamics simulation framework for an $Al+Fe_2O_3$ reactive metal powder mixture. In: Peter, M.A., Timothy, F., Amit, M., Rudd, R.E., Nanoscale Materials and Modeling-Relations Among Processing, Microstructure and Mechanical Properties, vol. 821, pp. 319–325.

Tomar, V., Zhou, M., 2006a. Classical molecular-dynamics potential for the mechanical strength of nanocrystalline composite *fcc*-$Al+\alpha$-$Fe_2O_3$. Phys. Rev. B 73 (1–16), 174116.

Tomar, V., Zhou, M., 2006b. Tension-compression strength asymmetry of nanocrystalline $\alpha$-$Fe_2O_3$+*fcc*-Al ceramic-metal composites. Appl. Phys. Lett. 88 (1–3), 233107.

Van Swygenhoven, H., Caro, A., 1997. Plastic behavior of nanophase Ni: a molecular dynamics computer simulation. Appl. Phys. Lett. 71 (12), 1652–1654.

Van Swygenhoven, H., Caro, A., 1998. Plastic behavior of nanophase metals studied by molecular dynamics. Phys. Rev. B 58 (17), 11246–11251.

Van Swygenhoven, H., Spaczer, M., Caro, A., Farkas, D., 1999. Competing plastic deformation mechanisms in nanophase metals. Phys. Rev. B 60, 22–25.

Van Swygenhoven, H., Caro, A., Farkas, D., 2001. A molecular dynamics study of polycrystalline *fcc* metals at the nanoscale: grain boundary structure and its influence on plastic deformation. Mater. Sci. Eng. A 309–310, 440–444.

Van Swygenhoven, H., Derlet, P.M., FrØseth, A.G., 2004. Stacking fault energies and slip in nanocrystalline metals. Nat. Mater. 3, 399–403.

Van Swygenhoven, H., Derlet, P.M., Frøseth, A.G., 2006. Nucleation and propagation of dislocations in nanocrystalline *fcc* metals. Acta Mater. 54, 1975–1983.

Vincent, J., Merz, K.M., 1995. A highly portable parallel implementation of AMBER using the Message Massing Interface standard. J. Comp. Chem. 11, 1420–1427.

Voronoi, G.F., 1908. Nouvelles applications des parameters continus a la theorie des formes quadratiques. J. Reine Angew. Math. Premiere Memoire 133, 97–178.

Voter, A.F., Chen, S.P., 1987. Interatomic potentials for Ni, Al and $Ni_3Al$. Mater. Res. Soc. Symp. Proc. 82, 175–180.

Wolf, D., 1992. Reconstruction of NaCl surfaces from a dipolar solution to the Madelung problem. Phys. Rev. Lett. 68 (22), 3315–3318.

Yamakov, V., Wolf, D., Phillpot, S.R., Gleiter, H., 2002a. Deformation twinning in nanocrystalline Al by molecular dynamics simulation. Acta Mater. 50, 5005–5020.

Yamakov, V., Wolf, D., Phillpot, S.R., Gleiter, H., 2002b. Grain-boundary diffusion creep in nanocrystalline palladium by molecular dynamics simulation. Acta Mater. 50, 61–73.

Yamakov, V., Wolf, D., Phillpot, S.R., Mukherjee, A.K., Gleiter, H., 2004. Deformation-mechanism map for nanocrystalline metals by molecular-dynamics simulation. Nat. Mater. 3, 43–47.

Zhou, M., 2003. A new look at the atomic level virial stress on continuum-molecular system equivalence. Proc. Royal Soc. London A 459, 2347–2392.

Zhou, M., McDowell, D.L., 2002. Equivalent continuum for dynamically deforming atomistic particle systems. Philos. Mag. A 82 (13), 2547–2574.

Zimmerman, J.A., Kelchner, C.L., Klein, P.A., Hamilton, J.C., Foiles, S.M., 2001. Surface step effects on nanoindentation. Phys. Rev. Lett. 87 (16), 165504–165507.